J. Fluid Mech. (2010), *vol.* 661, *pp.* 130–158.
doi:10.1017/S0022112010003204

Elliptical instability in rotating cylinders: liquid metal experiments under imposed magnetic field

W. HERREMAN[1,2]†, D. CEBRON[2], S. LE DIZÈS[2] AND P. LE GAL[2]

[1]LRA, Ecole Normale Supérieure, 24, rue Lhomond, F-75005 Paris, France

[2]IRPHE, CNRS, Aix-Marseille Université, 49, rue Joliot Curie, F-13013 Marseille, France

(Received 17 December 2009; revised 9 June 2010; accepted 10 June 2010;
first published online 23 August 2010)

In this paper, we present new theoretical and experimental results on the elliptical instability in a liquid metal contained in a rotating deformable cylinder in the presence of an imposed magnetic field. The imposed field, which is aligned with the rotating axis, has a double interest. On the one hand, it permits an analysis of the inertial waves excited by the elliptical instability by measuring their induced magnetic fields. On the other hand, it permits the control of the instability by acting on the Joule damping. In this paper, firstly an analytical calculation of the magnetic field induced by the flow and its associated Joule damping is presented. Also, the linear and weakly nonlinear theories of the elliptical instability are extended to include magnetic field effects. Then, the description of the experiments starts by the presentation of the effect of the imposed magnetic field strength. Close to the instability threshold, both super- and subcritical bifurcations are identified. When the imposed field is decreased, we observe a transition towards complex nonlinear evolutions that we describe with the help of two-dimensional phase diagrams. In a second set of experiments, we vary the eccentricity of the elliptic deformation over a large range in order to demonstrate that far from the instability threshold, the mean inertial wave amplitude is uncorrelated to the eccentricity. We show that, for a given eccentricity, this mean amplitude decreases when the rotation rate increases. In a last series of experiments, we focus on the description of the nonlinear evolution of an oscillatory eigenmode which is different from the principal stationary mode.

Key words: magnetic fluids, vortex instability

1. Introduction

The instability of flows with elliptic streamlines, named the elliptical instability, is recognized as a generic mechanism for the generation of small-scale turbulence in vortex systems (see for example the review of Kerswell 2002). The linear instability mechanism is understood as a parametric resonance of pairs of inertial waves. For small eccentricities, asymptotic theory leads to linear growth rate formulas, which are now available for many different elliptic vortices, in the presence of imposed magnetic fields (Kerswell 1993; Lebovitz & Zweibel 2004; Mizerski & Bayer 2009), density

† Email address for correspondence: wietze.herreman@lra.ens.fr

stratification (Miyazaki 1993) or thermal gradients (Le Bars & Le Dizès 2006). These theoretical results have been confirmed by experimental studies in both confined (Malkus 1989) and open flows (Leweke & Williamson 1998). Also, it has been shown that this instability can be important in the geophysical context of tidally deformed bodies (Kerswell 1994; Kerswell & Malkus 1998). Weakly nonlinear theories have been made for the flow in a cylinder (Waleffe 1989; Racz & Scott 2008) and for open flows (Sipp 2000), but very few numerical results have been able to confirm these theories as a much richer dynamics is usually obtained (Mason & Kerswell 1999; Schaeffer & Le Dizès 2010). In this paper, we use experiments to clarify some aspects of the nonlinear transition process.

A nice experimental set-up was invented by Malkus (1989) to study the elliptical instability. A rotating cylinder of liquid is elliptically deformed by a pair of opposed rollers so that the elliptic deformation is externally controlled. Theoretical analysis benefits from the relative simplicity of the expressions for the inertial waves in cylindrical geometry (Kelvin 1880). Early numerical results are also available in Mason & Kerswell (1999), but the most detailed information is in fact proposed by experimentalists. In a smaller but similar set-up to that of Malkus, Eloy, Le Gal & Le Dizès (2003) realized experimental observations that display quite good agreement with a weakly nonlinear model that describes the saturation of the elliptical instability. Further from threshold, the experiments revealed a violent secondary instability that leads to growth–collapse–relaminarization cycles. Note that similar inertial wave breakdowns were also observed in the case of precessing flows (Manasseh 1992) or when inertial waves are driven through boundary surface oscillations (McEwan 1970). Whereas the linear mechanism of the elliptical instability is now well known and confirmed, its complex nonlinear evolution still remains poorly understood. The current idea is that secondary instabilities such as triad resonances feed on the dominant inertial wave, bringing new frequencies into the flow and leading to a transition to chaos through the Ruelle–Takens transition scenario (Kerswell 2002). Up to now, most of the current data on the nonlinear evolution of the elliptical instability were produced by Kalliroscope visualization, a technique which is unfortunately very imprecise when small-scale structures are present in the flow. Some quantitative particle image velocimetry measurements have been performed by Eloy *et al.* (2003), but they have to cope with the complexity of the experimental set-up. Laser Doppler velocimetry measurements are successful in revealing long-term dynamics (Lacaze *et al.* 2006), but are often too noisy to describe rather complex dynamics in great detail. Ultrasound Doppler velocimetry achieves good accuracy in other experiments (Stefani *et al.* 2006; Schmitt *et al.* 2008), but achieving a contact between the probe and the rapidly rotating flow is experimentally not a simple task, in particular in small set-ups.

In this study, we use a new experimental set-up, named IMAGINE (an abbreviation for 'Instabilité MAgnéto INErtielle' in French) which was especially designed to study the nonlinear evolution of the elliptical instability. It is similar to the classical Malkus set-up, but it uses magnetic fields to detect the liquid metal (galinstan) motions under the application of an homogeneous magnetic field aligned along the rotation axis. Thus the inertial waves that are excited by the elliptical instability are accompanied by induced magnetic fields, which are detected outside the cylinder by high-sensitivity Hall probes. When the imposed field is small, this detection results in a quantitative indirect measure of the fluid motions inside the cylinder. When the field is large, Joule dissipation becomes important and adds a supplementary damping to the inertial waves. Note that magnetic field detection was already successfully used to observe

inertial waves excited by differential rotation in a large spherical Couette flow set-up (Kelley *et al.* 2007). Also note that as geostrophic flows do not induce magnetic fields, this technique permits a focus on inertial waves only. In previous works, a study of the elliptical instability has already been performed in spherical geometry, under weak and strong imposed fields (Lacaze *et al.* 2006; Herreman, Le Bars & Le Gal 2009). Time series of induced magnetic fields, have provided detailed information about the nonlinear evolution of the principle stationary mode (the spinover mode) that compares well with a low-dimensional theoretical model.

Here, we perform a similar study in cylindrical geometry. Our purpose is to increase our understanding of the transition towards the complex nonlinear states that have been studied in different previous works (Malkus 1989; Mason & Kerswell 1999; Eloy *et al.* 2003). We will produce and analyse data in the form of induced magnetic field time series, and we will show that Joule damping can be used as a way to control the complexity of the nonlinear state.

The article is organized as follows. We first describe the experimental set-up in § 2. Section 3 is then devoted to the theoretical analysis. After properly defining the problem, we calculate the magnetic fields induced by inertial waves and the way they are damped by the imposed field. We then use these results to add the magnetic field damping to the linear stability theory. We finally discuss the nonlinear evolution in a qualitative way, and highlight the role of detuning for the criticality of the elliptical instability bifurcation. The experimental results are presented in § 4. Section 4 is split in four subsections. Sections 4.1–4.3 focus on the dominant stationary mode of the elliptical instability and analyse the effects of varying magnetic field strength, varying eccentricity and varying rotation rate. Section 4.4 considers the nonlinear evolution of another elliptical instability mode. Some conclusions are finally drawn in § 5.

2. The experimental set-up 'IMAGINE'

Figure 1 presents a photograph and a schematic representation of our experimental set-up. It is a modified version of Malkus' set-up (Malkus 1989; Eloy *et al.* 2003) specifically adapted to magnetic-field-detection purposes. All moving components other than the liquid metal are cast from insulating materials. The working fluid is galinstan, a gallium–indium–tin eutectic which is liquid at room temperature. Its physical properties are $\rho = 6440\,\mathrm{kg\,m^{-3}}$ for the density, $\nu = 0.93 \times 10^{-6}\,\mathrm{m^2\,s^{-1}}$ for its kinematic viscosity and $\sigma_e = 3.41 \pm 0.5 \times 10^6\,\mathrm{S\,m^{-1}}$ for its electrical conductivity (D. Charalampous, E. Dubois & J. Chevalet, private communication, 2009). The vacuum magnetic permeability is denoted μ_0.

The fluid is contained in a deformable cylindrical container (see label '1' in figure 1) with an inner radius $R = 25 \pm 0.5\,\mathrm{mm}$. The PVC tubes of Eloy *et al.* (2003) are used as elastic but resistant envelopes, surrounding a soft but impermeable thin silicone inner cylinder of thickness 2 mm. The purpose of this inner envelope is to ensure a good sealing of the whole system. The cylinder is closed with plastic top and bottom lids. The height H of the cylinder can be adjusted within the range $[120, 160]$ mm. The cylinder rotates at an angular velocity Ω between 0 and 5 Hz, guided in a set of ceramic bearings. The elliptic deformation is imposed by two opposed teflon rollers (see '2' in figure 1) mounted also on ceramic bearings. The eccentricity ϵ of the elliptic deformation can be varied during the experiment in the range $[0, 0.3]$. The cylinder is mounted between two water-cooled Helmholtz coils (see '3' in figure 1) that are fixed to two parallel soft-iron plates (see '4' in figure 1) of thickness 20 mm. The high relative magnetic permeability ($\mu_{Fe}/\mu_0 \simeq 700$) of these plates increases the intensity

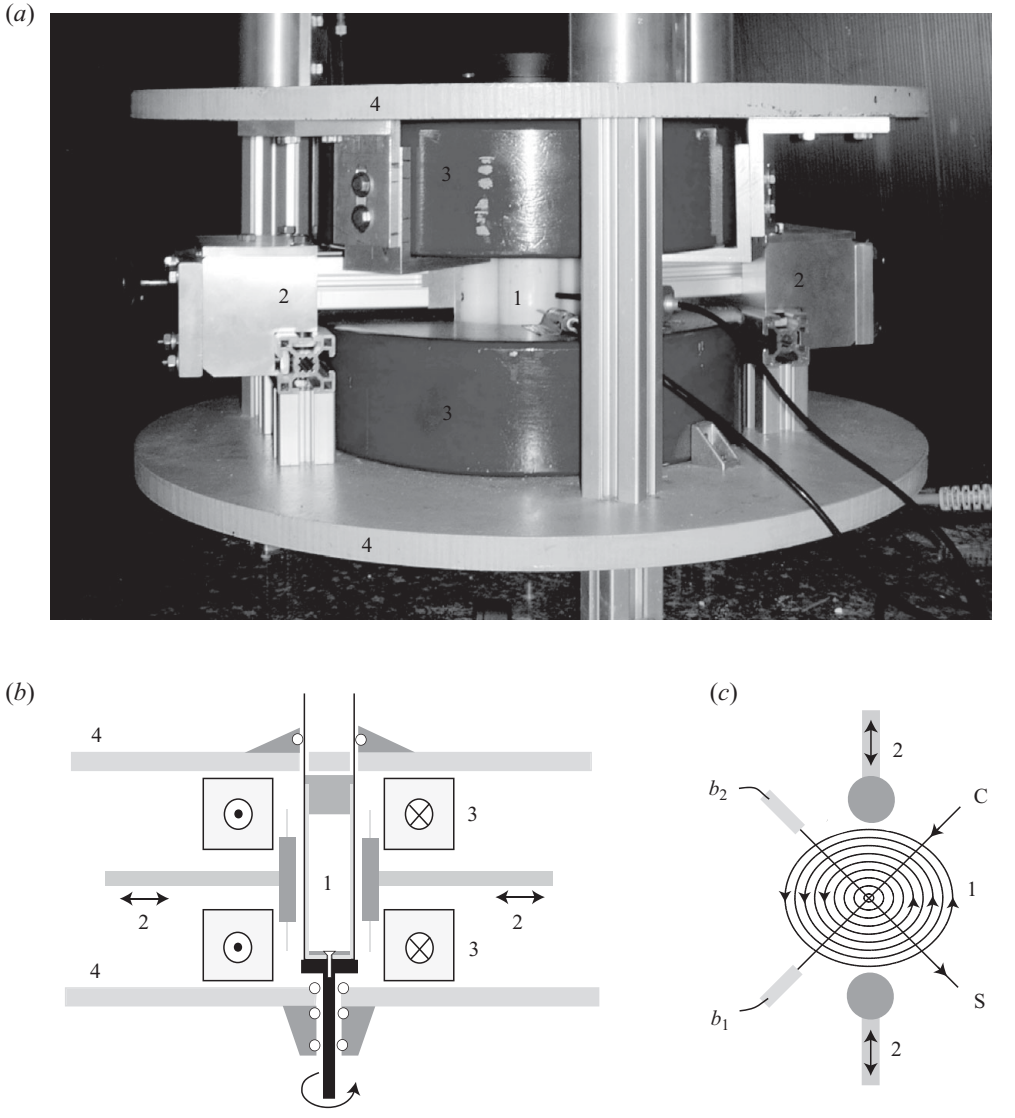

FIGURE 1. Photograph and schematic representation of the IMAGINE set-up. (1) Elliptically deformed rotating cylinder full of galinstan liquid metal. (2) Opposed rollers for elliptic deformation. (3) Helmholtz coils. (4) Iron plates. Two Hall probes b_1 and b_2 are placed in the equatorial plane of the cylinder and measure radial field components along the directions C and S, respectively, $\pm 45°$ from the short axis of the elliptical cross-section.

and the homogeneity of the imposed field, and shelters the experiment from outside magnetic field noise. The distance between horizontal endplates of the galinstan cylinder and the iron plates is 20–50 mm depending on the length of the cylinder. The 160 mm inner diameter coils are powered by a stabilized DC supply. We can impose the field intensity B_0 in the interval $[0, 0.12]$ T. The FEMM-freeware package for magnetostatics was used to study the field-homogeneity, which is optimized in the central part of the set-up. The ensemble is fixed to a heavy granite table, under which a 600-W AC motor is positioned to drive the rotation axis of the cylinder. The rotation speed is digitally controlled with an accuracy better than 1 %.

The theoretical analysis that will be presented in § 3, provides an estimate of the typical amplitude b/B_0 of the field induced by the inertial waves which is of order $O(10^{-4})$. Consequently, an efficient detection of such small fields imposes severe constraints on the magnetic field probes which should not be perturbed by the much larger field imposed along the axis. In this study, we use a set of three Hall-effect probes with a maximum sensitivity of 300 μT/mV (FW-Bel-Sypris – Model 7030). A first probe measures the imposed magnetic field B_0 along the axis. Two other probes are placed in the equatorial plane of the cylinder. The signal denoted b_1 records the radial field component along the direction (C) (see top view of the sketch in figure 1), -45° away from the short axis of the elliptical cross-section in the rotation sense. The second identical probe b_2 measures the radial field component in the direction (S) at $+45^\circ$. These directions correspond to the principal directions of the strain field induced by the rollers, as explained in § 3. Both probes are about 1 ± 0.5 mm away from the external boundary of the rotating cylinder. This distance does not vary significantly for different eccentricities, mainly because the probes are in the $\pm 45^\circ$ directions where the cross-section is close to that of the undeformed cylinder. The misalignment of the probes does not exceed 5° for each probe. The homogeneity of the imposed field cannot be guaranteed up to the required $O(10^{-4})$ precision levels. As a result the radial probes in the equatorial plane see a small stationary field. This constant signal is easily subtracted before each experiment, by changing the offset of the probes. The remaining signal is then amplified by a factor 100–200, and low-pass filtered with a cutoff frequency f_c between 4 and 20 Hz, before being recorded by the data-acquisition unit. Numerical filtering is then preferred to reveal the very slow dynamics of the signals.

3. Theoretical analysis

Elliptical instability in the Malkus' (1989) set-up has previously received much attention, especially in Waleffe (1989) hereafter referred to as W89, Mason & Kerswell referred to as MK99 and Eloy *et al.* (2003) referred to as E03. After defining the problem and the notation, we calculate the magnetic field induced by inertial waves and their magnetic damping. Then we use this information to extend the linear instability theory and finally discuss some qualitative aspects of the nonlinear evolution of the instability.

3.1. *Base state and perturbation problem*

The liquid metal is confined in an elliptically deformed cylinder. The elliptical sidewall of this fluid domain can be parametrized as

$$\frac{x^2}{1+\epsilon} + \frac{y^2}{1-\epsilon} = R^2, \quad z \in [0, H], \tag{3.1}$$

in Cartesian coordinates (x, y, z). The two horizontal top and bottom plates that close the cylinder are placed at $z = 0$ and $z = H$. The eccentricity is positive $0 < \epsilon < 1$, so that the x-axis is the long axis of the ellipse while the y-axis is its short axis (as shown in figure 1). If we spin up a fluid inside this deformed cylinder, we can realize a flow with elliptical streamlines of same eccentricity as the boundary:

$$\boldsymbol{U}_0 = \Omega \left[-\sqrt{\frac{1+\epsilon}{1-\epsilon}}\, y\hat{\boldsymbol{x}} + \sqrt{\frac{1-\epsilon}{1+\epsilon}}\, x\hat{\boldsymbol{y}} \right] \tag{3.2a}$$

$$= \Omega \left[(-y\hat{\boldsymbol{x}} + x\hat{\boldsymbol{y}}) - \epsilon(y\hat{\boldsymbol{x}} + x\hat{\boldsymbol{y}}) + O(\epsilon^2) \right]. \tag{3.2b}$$

We denote $\hat{\boldsymbol{x}}, \hat{\boldsymbol{y}}, \hat{\boldsymbol{z}}$ the Cartesian unit vectors. For small ϵ, we see from (3.2*b*) that the elliptical flow is composed of a dominant solid body rotation and an ϵ times smaller strain field that stretches the direction (S) at angles $-\pi/4, 3\pi/4$ away from the x-axis and compresses the direction (C) at angles $+\pi/4, -3\pi/4$ from the x-axis (see figure 1). The homogeneous magnetic field $\boldsymbol{B}_0 = B_0\,\hat{\boldsymbol{z}}$ imposed along the rotation axis, does not interact with this two-dimensional elliptic flow. Thus $\boldsymbol{U}_0$ and $\boldsymbol{B}_0$ define an exact magnetohydrodynamic (MHD) base state.

From previous studies on the elliptical instability, we know that an elliptical flow is often unstable. Pairs of inertial waves can mutually amplify each other through a vorticity-stretching mechanism (see W89). Formally, the instability can be modelled as a parametric resonance of inertial waves. Here we want to know how the imposed field modifies the elliptical instability, and how we can follow the instability through the induced magnetic fields that are measured outside the cylinder.

To keep track of the elliptical instability in the analysis, we introduce perturbation fields $\boldsymbol{u}$ and $\boldsymbol{b}$ that add onto the base state. In the following, we will use non-dimensional variables. Space, time and velocity fields will be scaled in units

$$[\boldsymbol{r}] = R, \quad [\boldsymbol{t}] = \Omega^{-1}, \quad [\boldsymbol{u}] = [\boldsymbol{U}_0] = \Omega R. \tag{3.3}$$

We denote by $h = H/R$ the aspect ratio of the cylinder. The scale of the imposed field is of course $[\boldsymbol{B}_0] = B_0$, but for the magnetic field perturbations $\boldsymbol{b}$, we will use a different scale that involves the small magnetic Reynolds number (based on the rotation)

$$[\boldsymbol{b}] = Re_m\, B_0, \quad \text{with} \quad Re_m = \sigma_e\, \mu_0 \Omega R^2 \ll 1. \tag{3.4}$$

This scale is well adapted to describe magnetic field perturbations in the quasi-static or resistive limit of MHD. In this limit, magnetic field diffusion is so strong, that magnetic field advection and Alfvén waves can be neglected. This requires that both Re_m and the Lundquist number $S = \sigma_e \sqrt{\mu_0} B_0 R/\sqrt{\rho}$ are small compared to unity, which is the case in our set-up.

To cope with the elliptical deformation of the boundaries, we follow previous works on the elliptical instability (Bayly 1986; Vladimirov & Vostretsov 1986; W89; MK99) by introducing the non-orthogonal elliptico-polar system (s, ϕ, z). These coordinates are related to the Cartesian coordinate system as

$$x = s\sqrt{1+\epsilon}\cos\phi, \quad y = s\sqrt{1-\epsilon}\sin\phi. \tag{3.5}$$

The associated (non-normalized) vectors are denoted

$$\tilde{\boldsymbol{s}} = \sqrt{1+\epsilon}\cos\phi\,\hat{\boldsymbol{x}} + \sqrt{1-\epsilon}\sin\phi\,\hat{\boldsymbol{y}}, \tag{3.6a}$$

$$\tilde{\boldsymbol{\phi}} = -\sqrt{1+\epsilon}\sin\phi\,\hat{\boldsymbol{x}} + \sqrt{1-\epsilon}\cos\phi\,\hat{\boldsymbol{y}}. \tag{3.6b}$$

The elliptico-polar coordinate system maps the elliptical boundary (3.1) on the coordinate surface $s = 1$, and the base flow on the simple flow $\boldsymbol{U}_0 = s\tilde{\boldsymbol{\phi}}$, which explains why they are so well-adapted. Perturbation fields will be expanded as

$$\boldsymbol{u} = u_s\tilde{\boldsymbol{s}} + u_\phi\tilde{\boldsymbol{\phi}} + u_z\hat{\boldsymbol{z}}, \tag{3.7}$$

and similarly for $\boldsymbol{b}$. The non-orthogonal transform introduces additional terms in the equations through the spatial derivatives. However, the relations $\partial_\phi\tilde{\boldsymbol{s}} = \tilde{\boldsymbol{\phi}}$ and $\partial_\phi\tilde{\boldsymbol{\phi}} = -\tilde{\boldsymbol{s}}$ still hold as if (s, ϕ, z) were ordinary cylindrical coordinates, and as a consequence the relation

$$\nabla\cdot\boldsymbol{u} = \left(\partial_s + \frac{1}{s}\right)u_s + \frac{1}{s}\partial_\phi u_\phi + \partial_z u_z = 0, \tag{3.8}$$

and Gauss' law keep their simple form. Moreover, the nonlinear term $(\boldsymbol{u}\cdot\nabla)\boldsymbol{u}$ stays in its same simple form as in cylindrical coordinates (see MK99). The linearized perturbation equations for $\boldsymbol{u}$, $\boldsymbol{b}$, p inside the cylinder are at leading order

$$(\partial_t + \partial_\phi)\boldsymbol{u} + 2\,\hat{\boldsymbol{z}}\times\boldsymbol{u} + \nabla p = \epsilon\,\mathscr{E}\,\nabla p + E\,\Delta\boldsymbol{u} + \Lambda\,\partial_z\boldsymbol{b}, \tag{3.9a}$$

$$\Delta\boldsymbol{b} + \partial_z\boldsymbol{u} = 0, \tag{3.9b}$$

$$\nabla\cdot\boldsymbol{u} = \nabla\cdot\boldsymbol{b} = 0. \tag{3.9c}$$

The operators ∇ and Δ are the ordinary cylindrical gradient and Laplacian operators. The pressure p in (3.9a) is a modified pressure which includes a $-\Lambda b_z$ term that comes from the Lorentz force. The Ekman number E and Elsasser number Λ which are defined by

$$E = \frac{\nu}{\Omega R^2} \ll 1, \quad \Lambda = \frac{\sigma_e B_0^2}{\rho\,\Omega}, \tag{3.10}$$

measure the importance of viscous effects and of the Lorentz force, respectively. The leading order term that captures the effect of the elliptical deformation, involves only the pressure variable

$$\mathscr{E}\nabla p = \frac{1}{2}\left[\mathrm{e}^{\mathrm{i}2\phi}\left(\partial_s p + \frac{\mathrm{i}}{s}\partial_\phi p\right)(\tilde{\boldsymbol{s}} + \mathrm{i}\tilde{\boldsymbol{\phi}}) + \mathrm{e}^{-\mathrm{i}2\phi}\left(\partial_s p - \frac{\mathrm{i}}{s}\partial_\phi p\right)(\tilde{\boldsymbol{s}} - \mathrm{i}\tilde{\boldsymbol{\phi}})\right]. \tag{3.11}$$

Higher-order contributions such as elliptico-viscous terms $O(\epsilon E)$, the advective terms $Re_m(\partial_t + \partial_\phi)\boldsymbol{b}$, and the terms that capture elliptical deformation of the magnetic field are all neglected.

With the magnetic field probes placed outside the cylinder, we need to solve $\boldsymbol{b}$ also outside the cylinder. In the isolating external region, the magnetic field perturbation is properly described by a magnetic potential Φ which satisfies

$$\Delta\Phi = 0, \quad \boldsymbol{b} = \nabla\Phi. \tag{3.12}$$

Elliptical deformations of the external field do not add leading order contributions, and are neglected in what follows.

The proper boundary conditions for this problem are no-slip boundary conditions for $\boldsymbol{u}$, and continuity of $\boldsymbol{b}$ on the boundary surface. Imposing this magnetic boundary condition for a cylinder surrounded by air is a difficult task. To make the analysis possible, we will suppose idealized ferromagnetic ($\mu\to\infty$) boundaries at $z=0$ and h, both inside and outside the fluid domain. The field $\boldsymbol{b}$ is then normal to these plates. On the elliptical surface we still impose field continuity.

High-permeability plates are present in the experimental set-up, but they are not in direct contact with the fluid. The magnetic fields that will be calculated are thus not exactly identical to the real induced fields in the set-up. However, we find good approximations of the fields at the position of the probes. Since the exterior field-potential Φ satisfies a Laplacian problem (3.12), its value entirely depends on the potential at the boundary. Then we can see this boundary as a superposition of point sources at positions r_s, each of them having a Green's function contribution that decays as $|r_s - r_0|^{-1}$ to the potential $\Phi(r_0)$. From this, we understand that probes positioned close to the boundary surface, are mainly influenced by nearby boundary points, whatever the precise nature of far away boundary conditions might be. We expect larger errors localized close to corner regions of the cylinder.

3.2. *Inertial waves, induced fields and magnetic damping*

Now we solve this problem in the limit of small ϵ, E and Λ using a perturbation approach. This starts with the linearized unperturbed problem: in (3.9) we neglect all terms on the right-hand side (ϵ, E, $\Lambda \to 0$). We use the boundary conditions

$$u_z = 0, \quad \text{at} \quad z = 0, h, \qquad u_s = 0, \quad \text{at} \quad s = 1, \tag{3.13a}$$

$$\hat{\boldsymbol{z}} \times \boldsymbol{b} = 0, \quad \text{at} \quad z = 0, h, \qquad \boldsymbol{b}^{int} = \boldsymbol{b}^{ext}, \quad \text{at} \quad s = 1. \tag{3.13b}$$

The no-slip condition needs to be relaxed for non-viscous flows. This problem is best solved using $(+, -, z)$ components instead of elliptico-polar components. They are related to each other by

$$u_\pm = (u_s \pm \mathrm{i}u_\phi)/\sqrt{2}, \quad b_\pm = (b_s \pm \mathrm{i}b_\phi)/\sqrt{2}. \tag{3.14}$$

Writing down equations for $\pm$ parts of the fields, one notices that both the Coriolis term and the Laplacian operator are diagonal, which simplifies the calculations.

In the limit of a negligible magnetic field strength ($\Lambda \to 0$), it is clear that the solutions for the perturbation flows $\boldsymbol{u}$ are the purely hydrodynamic inertial waves, also known as Kelvin waves (Kelvin 1880)

$$\begin{bmatrix} u_\pm \\ u_z \\ p \end{bmatrix} = A \begin{bmatrix} (2 \mp \lambda)/\sqrt{2} & J_{m\pm1}(ks) & \cos(lz) \\ k\lambda/l & J_m(ks) & \sin(lz) \\ \mathrm{i}k\lambda^2/l^2 & J_m(ks) & \cos(lz) \end{bmatrix} \mathrm{e}^{\mathrm{i}(m\phi+\omega t)}, \tag{3.15}$$

where J_m stands for ordinary Bessel functions, $A = |A|\mathrm{e}^{\mathrm{i}\chi}$ is an arbitrary complex amplitude, $k \in \mathbb{R}$, $m \in \mathbb{Z}$ and $l \in \mathbb{R}$ are the radial, azimuthal and vertical wavenumbers, respectively, and ω is the fixed frame frequency. The parameter $\lambda = m + \omega$ is the rotating frame frequency in the range $\lambda \in [-2, 2]$. Only waves with particular wavenumbers can satisfy the boundary condition (3.13*a*). This constraint is captured in the dispersion relation

$$\lambda^2 = \frac{4l^2}{k^2 + l^2}, \quad (2+\lambda)J_{m-1}(k) + (2-\lambda)J_{m+1}(k) = 0, \quad l = n\pi/h, \tag{3.16}$$

where $n \in \mathbb{N}$ is the number of half vertical wavelengths in the flow.

We now calculate the magnetic field induced by such Kelvin waves, as the solution of the Poisson problem (3.9*b*). The field inside the cylinder is composed of a forced part and a homogeneous part $\boldsymbol{b} = \boldsymbol{b}^{(f)} + \boldsymbol{b}^{(h)}$. The forced field $\boldsymbol{b}^{(f)}$ is a particular solution that we find here as

$$\begin{bmatrix} b_\pm^{(f)} \\ b_z^{(f)} \end{bmatrix} = \frac{A\,l}{k^2 + l^2} \begin{bmatrix} -(2 \mp \lambda)/\sqrt{2} & J_{m\pm1}(ks) & \sin(lz) \\ k\lambda/l & J_m(ks) & \cos(lz) \end{bmatrix} \mathrm{e}^{\mathrm{i}(m\phi+\omega t)}. \tag{3.17}$$

Interestingly, this field immediately respects the ideal boundary condition (3.13*b*), which explains why this idealized condition is so well-adapted. (Remark that this would not be the case for perfectly conducting plates with $\sigma_e \to 0$, which require the field to be tangential to the surface.) We further note that the factor $A\,l\,(k^2+l^2)^{-1}$ fixes the amplitude of the induced fields, and that this factor decays for modes with smaller scales (larger k and l). The homogeneous solution $\boldsymbol{b}^{(h)}$ of the Laplacian problem is necessary to link inner and outer fields at $s = 1$. We find

$$\begin{bmatrix} b_\pm^{(h)} \\ b_z^{(h)} \end{bmatrix} = \frac{A\,l}{k^2 + l^2} \begin{bmatrix} d_\pm & I_{m\pm1}(ls) & \sin(lz) \\ \dfrac{1}{\sqrt{2}}(d_+ + d_-) & I_m(ls) & \cos(lz) \end{bmatrix} \mathrm{e}^{\mathrm{i}(m\phi+\omega t)}. \tag{3.18}$$

Here $d_\pm$ are two arbitrary constants that will be fixed by the boundary conditions, and I_m is a modified Bessel function of the first kind. Outside the cylinder, the magnetic field and its potential are given by

$$\begin{bmatrix} \Phi \\ b_\pm \\ b_z \end{bmatrix} = c\frac{A\,l}{k^2+l^2} \begin{bmatrix} \dfrac{1}{l} & K_m(ls) & \sin(lz) \\ -\dfrac{1}{\sqrt{2}} & K_{m\pm1}(ls) & \sin(lz) \\ & K_m(ls) & \cos(lz) \end{bmatrix} \mathrm{e}^{\mathrm{i}(m\phi+\omega t)}. \tag{3.19}$$

Here c is a third arbitrary constant and K_m is a modified Bessel function of the second kind. The three coefficients c and $d_\pm$ are uniquely determined by expressing the three relations that follow from the field continuity at $s=1$.

Up to this point, we have neglected the Lorentz force. The Elsasser number is not necessarily small in the experiment, $\Lambda = O(1)$ and so we might wonder how this force modifies the inertial waves. To find an answer to this question, we solve (3.9) still in the limit $(\epsilon, E \to 0)$, but keeping the Lorentz-force term. This requires (3.9*a*) and (3.9*b*) to be solve simultaneously, which seems *a priori* to render the problem more complex. Surprisingly, it turns out that this is not the case. We find that the Lorentz force does not modify the spatial structure of the waves: both $\boldsymbol{u}$ and $\boldsymbol{b}$ are given by the previous formulas (3.15) to (3.19). The waves are, however, no longer neutral: the Lorentz force introduces a damping that modifies the time-dependence of the waves into

$$\mathrm{e}^{\mathrm{i}\tilde{\omega}t}, \quad \text{with} \quad \tilde{\omega} = \omega + \mathrm{i}\Lambda\frac{l^2}{k^2+l^2} = \omega + \mathrm{i}\Lambda\frac{\lambda^2}{4}. \tag{3.20}$$

Unlike in the ideal MHD limit (Kerswell 1993), the frequency of the waves is not modified by the magnetic field in the resistive limit of MHD, $\mathrm{Re}(\tilde{\omega}) = \omega$. The only effect of the imposed field is a magnetic damping that increases linearly with the Elsasser number Λ. We see that this damping only depends on the ratio k/l of the waves, or using the dispersion relation (3.16), only on the square of the rotating frame frequency λ. From now on, we will only be concerned with the case $\Lambda = O(\epsilon)$, where the elliptical instability can be strong enough to overcome the magnetic field damping.

In the previous calculations, we have neglected the viscous boundary layers of thickness $O(E^{1/2})$. These layers do not add significant contributions to the induced field, whenever $\Lambda \ll 1$ which it is the case of concern. We finally note that geostrophic modes without any vertical structure, $\partial_z \boldsymbol{u} = 0$, do not induce magnetic fields and are thus not damped by the imposed field.

3.3. *Linear theory of the elliptical instability*

We now model the effect of elliptical, viscous and Lorentz forces in a perturbative way. Problems (3.9)–(3.12) are written in the short form

$$\mathscr{L}\boldsymbol{X} = \epsilon\mathscr{D}\boldsymbol{X} + E\mathscr{V}\boldsymbol{X} + \Lambda\mathscr{M}\boldsymbol{X}. \tag{3.21}$$

Here, $\boldsymbol{X} = [\boldsymbol{u}, p, \boldsymbol{b}, \Phi]^{\mathrm{T}}$ is a vector gathering together all fields of the problem. The operator $\mathscr{L}$ contains the left-hand side of (3.9), the incompressibility relation and the external problem (3.12). Operators $\mathscr{D}$, $\mathscr{V}$ and $\mathscr{M}$ capture the elliptical, viscous and Lorentz force perturbations, respectively, that can be inferred from the right-hand side of (3.9).

Section 2 solved the unperturbed problem $\mathscr{L}\boldsymbol{X} = 0$. We denote the different solutions for inertial waves and induced fields as $\boldsymbol{Q}_j(\boldsymbol{r})\,\mathrm{e}^{\mathrm{i}\omega_j t}$, where $\boldsymbol{Q}_j(\boldsymbol{r})$ gathers together the spatial structure of the fields and ω_j the frequencies. The elliptical term (3.11) couples

two inertial waves with wavenumbers and frequency $(k_j, m_j, l_j, \omega_j)$ resonantly when

$$m_1 + 2 = m_2, \quad l_1 = l_2, \quad \omega_1 = \omega_2, \quad k_1 \simeq k_2. \tag{3.22}$$

From the dispersion relation of the inertial waves (3.16), it is clear that these conditions can only be satisfied by very particular pairs of waves. The constraint on the radial wavenumbers $k_1 \simeq k_2$ is less strong, but selects the 'principal' modes that will always have significantly larger growth rates. These modes also have rotating frame frequencies $-\lambda_1 \simeq \lambda_2 \simeq 1$. Exact values for the wavenumbers and frequencies of the principal modes are reported in E03. We follow their notation (m_1, m_2, i) to refer to different principal modes where the index i is an integer measuring the number of radial oscillations of the mode. In reality, we need to account for the possibility of imperfect or detuned resonances, $\omega_1 \simeq \omega_2$. This is precisely measured by the so-called frequency detuning

$$\delta = \epsilon\, \delta' = \frac{(\omega_1 - \omega_2)}{2}, \tag{3.23}$$

which should not be much larger than ϵ. This frequency detuning can be related to a geometrical detuning coming from the aspect ratio of the cylinder. Perfect resonant modes require a very particular vertical wavenumber $l_1 = l_2 = l_*$, so that they can only exist in cylinders with aspect ratios $h_* = n\pi/l_*$. Detuned resonances exist within a range $\Delta h/h_* \sim \epsilon$ around h_*. We now build an asymptotic ansatz out of a pair of almost resonant waves

$$\boldsymbol{X} = \left(A_1 \boldsymbol{Q}_1 + A_2 \boldsymbol{Q}_2\right) \mathrm{e}^{\mathrm{i}\bar{\omega} t + \epsilon \sigma' t} + \epsilon\, \boldsymbol{Y} + \cdots, \tag{3.24}$$

with $A_j \in \mathbb{C}$ two unknown amplitudes, $\bar{\omega} = (\omega_1 + \omega_2)/2$ is the mean frequency and $\sigma = \epsilon\, \sigma'$ is the leading order growth rate. We further assume that viscous and magnetic perturbations are $O(\epsilon)$, so that we can rescale Ekman number and Elsasser number as $E = \epsilon\, E'$, $\Lambda = \epsilon\, \Lambda'$. Injecting the ansatz (3.24) in (3.21), we find at first order in ϵ

$$\begin{aligned} \mathscr{L}\boldsymbol{Y} + ((\sigma' - \mathrm{i}\delta')A_1 \boldsymbol{Q}_1 + (\sigma' + \mathrm{i}\delta')A_2 \boldsymbol{Q}_2)\, \mathrm{e}^{\mathrm{i}\bar{\omega} t} \\ = (\mathscr{D} + E'\, \mathscr{V} + \Lambda'\, \mathscr{M})(A_1 \boldsymbol{Q}_1 + A_2 \boldsymbol{Q}_2)\, \mathrm{e}^{\mathrm{i}\bar{\omega} t}. \end{aligned} \tag{3.25}$$

Magnetic, viscous and elliptical terms introduce secular forcings of the linear problem $\mathscr{L}\boldsymbol{Y}$. To cope with these terms, we need to set a solvability condition, that will lead us to the growth rate and the relation between A_1 and A_2. For this, we introduce a scalar product

$$\langle \boldsymbol{Q}_1 | \boldsymbol{Q}_2 \rangle = \int_{V_i} (\boldsymbol{u}_1^* \cdot \boldsymbol{u}_2 + p_1^*\, p_2 + \boldsymbol{b}_{i,1}^* \cdot \boldsymbol{b}_{i,2}) \mathrm{d}V + \int_{V_e} \Phi_1^*\, \Phi_2\, \mathrm{d}V, \tag{3.26}$$

and search for the adjoint modes. The adjoint operator $\mathscr{L}^A$ is found by partial integration

$$\left\langle \boldsymbol{Q}^A | \mathscr{L}\boldsymbol{Q} \right\rangle = \left\langle \mathscr{L}^A \boldsymbol{Q}^A | \boldsymbol{Q} \right\rangle + \mathrm{BT}, \tag{3.27}$$

and the adjoint modes solve $\mathscr{L}^A \boldsymbol{Q}^A = 0$, and satisfy boundary conditions that make the boundary terms (BT) in (3.27) vanish. We find here that

$$\boldsymbol{u}^A = \boldsymbol{u}, \quad \boldsymbol{b}^A = 0, \quad \Phi^A = 0. \tag{3.28}$$

The hydrodynamic field is self-adjoint as in the pure hydrodynamical case (W89, MK99 and E03), and the magnetic field part of the adjoint modes is zero. Perturbation couplings cannot arise through the elliptical deformation of the induction equation

in the resistive limit of MHD which further assures that the elliptical terms in the magnetic field equation of (3.9*b*) are not relevant. The solvability condition is expressed by $\langle \boldsymbol{Q}_j^{A*} | (3.25) \rangle$, for $j = 1, 2$ and uses the fact that $\langle \boldsymbol{Q}_j^{A*} | \mathscr{L} \boldsymbol{Y} \rangle = 0$. This leads to the algebraic system of equations

$$\left(\sigma - \mathrm{i}\delta + d_1^M + d_1^V\right) A_1 = \epsilon\, E_{12}\, A_2, \tag{3.29a}$$

$$\left(\sigma + \mathrm{i}\delta + d_2^M + d_2^V\right) A_2 = \epsilon\, E_{21}\, A_1. \tag{3.29b}$$

All matrix elements are specified in the appendices. The elliptic elements E_{12} and E_{21} are identical to the non-viscous values found in W89 and within $O(\epsilon)$ of those calculated in E03. (These authors modelled the elliptical deformation through boundary condition modifications, instead of using elliptico-polar coordinates.) We denote by d_j^V the viscous damping terms which capture both surface $O(E^{1/2})$ and volume damping $E(k_j^2 + l_j^2)$ that arises through the operator $\mathscr{V}$. The magnetic terms d_j^M are produced by the Lorentz force term $\mathscr{M}$. We find

$$d_j^M = \Lambda \frac{\lambda_j^2}{4}, \tag{3.30}$$

so that asymptotic modelling of the Lorentz force gives nothing but the exact answer (3.20). For the principal modes with $-\lambda_1 \simeq \lambda_2 \simeq 1$, the magnetic damping of both modes is identical $d_1^M = d_2^M = \Lambda/4$ at leading order. For these dominant modes, the final growth rate formula becomes

$$\sigma = -\frac{d_1^V + d_2^V}{2} + \sqrt{\epsilon^2\, E_{12}\, E_{21} - \left(\delta + \mathrm{i}\frac{d_1^V - d_2^V}{2}\right)^2} - \frac{\Lambda}{4}. \tag{3.31}$$

Compared to the purely hydrodynamical case, the only supplementary effect of the imposed magnetic field is a uniform magnetic field damping. A similar formula was found using a local instability analysis and for the principal stationary mode (spinover mode) in spheres (Thess & Zikanov 2007; Herreman, Le Bars & Le Gal 2009).

In figure 2, we have plotted the growth rate σ as a function of h for $\epsilon = 0.1$ and $E = 5 \times 10^{-4}$, for zero imposed field $\Lambda = 0$. This figure illustrates that different modes can be selected by tuning the aspect ratio h of the cylinders in the experiment, within $O(\epsilon)$ ranges of perfectly resonant aspect ratios h_*. Note that small viscous detuning ($\mathrm{Im}(d_j^V) \neq 0$), modifies the position of the peak from its non-viscous value. For the parameters of figure 2, the principal stationary mode $(-1, 1, 1)$ produces the tallest resonance horns centred around the aspect ratios $h_* = n\pi/1.58 \simeq 2n$. The other most important modes are (○), $(0, 2, 1)$, centred around $h_* = n\pi/2.33 \simeq 1.35n$, (□), $(1, 3, 1)$ around $h_* = n\pi/3.04 \simeq n$ and (●), $(-1, 1, 2)$ around $h_* = n\pi/3.29 \simeq 0.95n$. In the presence of an imposed magnetic field, the damping translates the diagram of figure 2 downwards over a distance $\Lambda/4\epsilon$. A critical Elsasser number Λ_c exists, beyond which all mode becomes linearly stable.

In the experiments, we will study configurations with aspect ratios around $h \simeq 6$, with $\epsilon \simeq 0.1$ and $E \simeq 10^{-4}$. We will concentrate mainly on the principal stationary resonance $(-1, 1, 1)$, which is always the most unstable mode according to theory. It consists of the resonance of the inertial wave $(k, m, l, \omega) = (2.73, 1, 1.58, 0)$ with amplitude $A = |A| \mathrm{e}^{\mathrm{i}\chi}$ and its complex conjugate. This mode is perfectly resonant in a cylinder with aspect ratio $h_* = 5.97$. The linear system (3.29) reduces to

$$\left(\sigma + \mathrm{i}\delta + \frac{\Lambda}{4} + d^V\right) A = \epsilon\, E_{1-1}\, A^*. \tag{3.32}$$

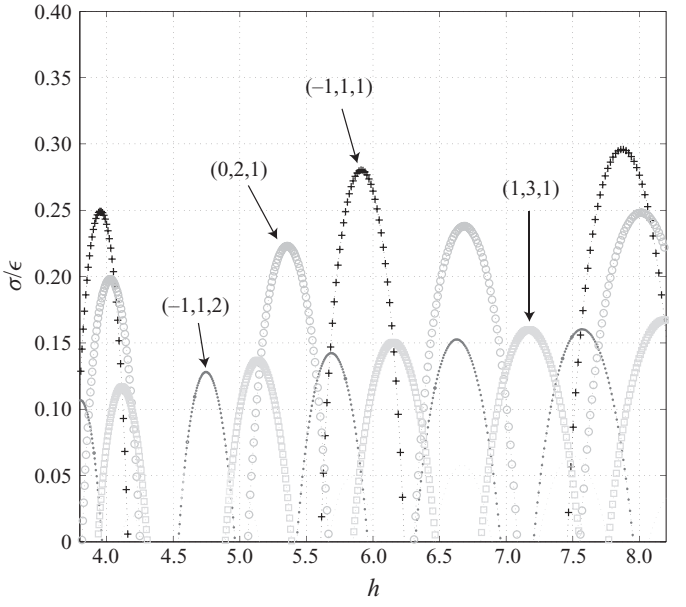

FIGURE 2. Growth rate of elliptic instability modes $(m, m+2, x)$ in a cylinder as a function of the aspect ratio h, for $\epsilon = 0.1$, $E = 5 \times 10^{-4}$. In the presence of a magnetic field, Joule damping uniformly lowers the growth rate of all elliptically unstable couplings by an amount of $-\Lambda/4$.

All matrix elements are explicitly given in the appendices. Note that $E_{1-1} = \mathrm{e}^{-\mathrm{i}\pi/2}|E_{1-1}|$. We deduce the following relations for σ and the phase χ of the unstable mode

$$\sigma = -\mathrm{Re}(d^V) + \sqrt{\epsilon^2\,|E_{1-1}|^2 - [\,\delta + \mathrm{Im}\,(d^V)\,]^2} - \frac{\Lambda}{4}, \tag{3.33}$$

$$\chi = -\arctan\sqrt{\frac{1+\kappa}{1-\kappa}} \quad \text{with} \quad \kappa = \frac{\delta + \mathrm{Im}(d^V)}{\epsilon|E_{1-1}|}. \tag{3.34}$$

The growth rate is maximal, when the frequency detuning $\delta_{tot} = \delta + \mathrm{Im}(d^V)$ vanishes. We find $\mathrm{Im}(d^V) = 0.393\,E^{1/2}$ so that δ needs to be negative to balance the viscous detuning: perfect resonance conditions for viscous flows require slightly shorter cylinders than predicted by the non-viscous theory. The phase at perfect resonance is always $\chi = -\pi/4$ or $\chi = 3\pi/4$. Note that the magnetic field does not modify χ.

Vorticity and induced magnetic field lines of the principal stationary mode at perfect resonance $\chi = -\pi/4$, are plotted in the mid-plane of the cylinder $z = 3$ in figure 3, using the results of § 2. As can be observed, the vorticity is indeed aligned with the axis of maximum stretching, as suggested by the physical mechanism. The magnetic field is dipolar with axis along the compressed direction. The symmetrical unstable mode with phase $\chi = 3\pi/4$, has the same picture with inverted arrows.

We have used this information to plan the experimental set-up. Positioning the radial Hall probes b_1 and b_2 as in figures 1 and 3, we can expect from linear theory, that the radial probe b_1 along the direction (C) measures a maximal signal strength, whereas the probe b_2 placed in direction (S) measures nothing when the system is at perfect resonance. Detuned resonances will be detected by the fact that b_2 is non-zero. To be more precise, we can combine both signals b_1 and b_2 to find a measure related

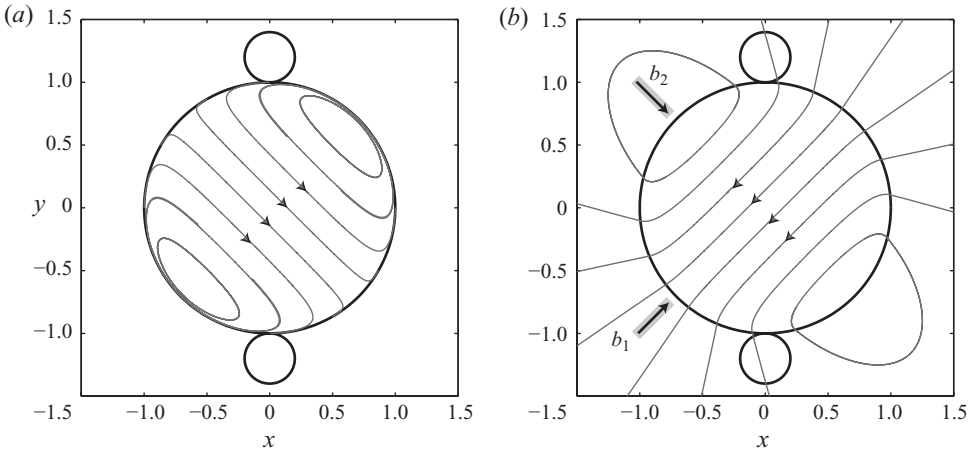

FIGURE 3. Vorticity (a) and induced magnetic field lines (b) in the equatorial plane $z=h/2$, for the principal stationary mode $(-1, 1, 1)$ in a cylinder of aspect ratio $h=6$. The circles on top and bottom indicate the location of the rollers. For clarity, the radial Hall probes b_1 and b_2 have been added to the picture.

to the phase of the principal stationary mode

$$\arctan(b_2/b_1) = \chi_{\exp} + \pi/4 - \frac{1-\mathrm{sgn}(b_1)}{2}\,\pi. \tag{3.35}$$

Growth rates can be measured on any of the signals b_1 and b_2 or $(b_1^2+b_2^2)^{1/2}$. When the rotation sense is modified in the experiment, stretched and compressed axes, and therefore the signals at probes b_1 and b_2 are inverted.

3.4. *Nonlinear evolution of the elliptical instability*

Whereas the linear theory of the elliptical instability has been confirmed by many independent studies, the nonlinear evolution of the instability still remains poorly understood. Most of our understanding results from weakly nonlinear models, first introduced in W89. MK99 then performed a detailed analysis for the saturated state of the principal stationary mode $(-1, 1, 1)$. The most recent results are from E03, who gave amplitude equations for the principal stationary mode and the nonlinearly excited geostrophic flow. This model can be easily extended to study how the magnetic field damping modifies the weakly nonlinear equilibrium. In the limit $\Lambda = O(\epsilon)$, the only term to be added to the model of E03 is the magnetic damping $-\Lambda/4$ of the mode $(-1, 1, 1)$. Geostrophic modes are not affected by supplementary damping or forcing terms. Equation (4.4a) of E03 for the amplitude a of the mode $(-1, 1, 1)$ is then

$$\partial_t a = (\epsilon\sigma_i \cos 2\varphi - E^{1/2}\mu_0 - \Lambda/4)a, \tag{3.36}$$

and the other equations for the phase φ of the mode $(-1, 1, 1)$ and for the amplitudes $a_0^{(i)}$, $i=1, 2, 3, 4$ of the geostrophic modes, are

$$\partial_t \varphi = \delta + Da^2 - \epsilon\,\sigma_i \sin 2\phi + \sum_{i=1}^{4} \xi^{(i)} a_0^{(i)}, \tag{3.37a}$$

$$\partial_t a_0^{(i)} = 2\epsilon\lambda_1^{(i)} a^2 \cos 2\varphi + E^{1/2}\lambda_2^{(i)} a^2 - E^{1/2}\mu_1^{(i)} a_0^{(i)}. \tag{3.37b}$$

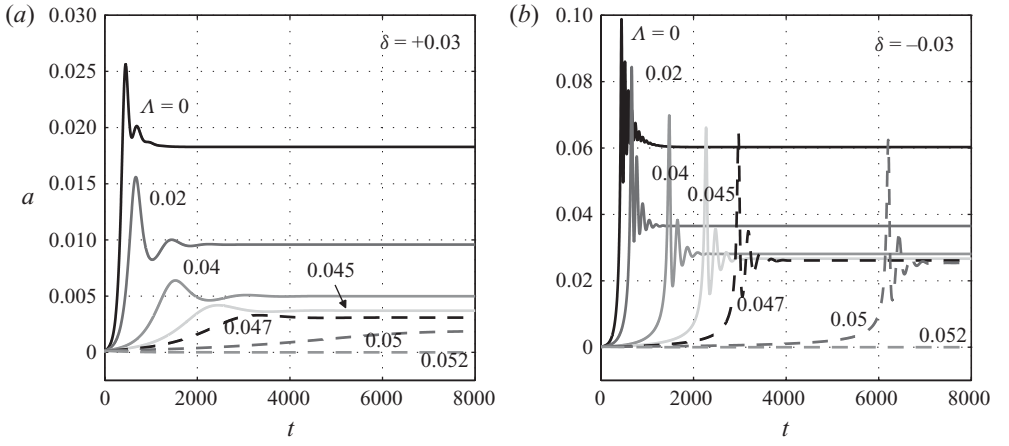

FIGURE 4. Weakly nonlinear dynamics of the principal stationary mode under an imposed field for different values of the Elsasser number Λ and for $\epsilon = 0.07$, $E = 10^{-4}$, $h \simeq 8$. Temporal evolution of the amplitude a. (a) Supercritical behaviour for positive frequency detuning δ. (b) Subcritical behaviour for negative frequency detuning δ.

The coefficients of (3.36) and (3.37a, b) were calculated by E03 for cylinders with $h \simeq 8$, and they are given in the appendices. We kept these values for the slightly shorter cylinders used here, as they are not expected to be dramatically changed, but also because we do not aim at full quantitative comparisons. The notations of E03 are translated into the notations used here, by the relation $|A| = ka$ for the principal resonance magnitude ($k = 2.73$). The phases are related by $\chi = -\varphi - \pi/4$.

We are also interested in the effect of the detuning δ. This is the only parameter that varies in the weakly nonlinear model when the aspect ratio of the cylinder is slightly different from the resonant value h_*. We always have $\delta > 0$ in a larger cylinder $h > h_*$, and inversely always $\delta < 0$ in shorter cylinders $h < h_*$.

In figure 4, we show some numerically calculated time-series for the magnitude a for two values of δ, corresponding to a slightly shorter cylinder ($\delta = -0.03$) and a slightly longer cylinder ($\delta = 0.03$). In the simulations, the initial value of the amplitude is fixed to 10^{-4} for the six variables of the model. As in the non-magnetic case, the system is always found to saturate. The stronger the field gets, the slower the initial exponential growth, and around $\Lambda = 0.052$, the system is linearly stable, whatever the sign of δ. Saturation levels of the modes do, however, strongly depend on the sign of δ. For $\delta = 0.03$, we see that a gradual increase of Λ decreases the saturation amplitudes to zero. For $\delta = -0.03$, this is not the case: around $\Lambda \simeq 0.051$, the saturation level abruptly jumps to zero.

A closer investigation shows that the sign of the frequency detuning δ controls the criticality of the elliptical instability bifurcation. This is more clearly visible in figure 5, which shows bifurcation diagrams for the saturated mode magnitude a as a function of the Elsasser number Λ for different δ. In the very strongly detuned case ($\delta = -0.045$), we observe that a stable upper branch continues to exist, even though the system is now linearly stable for all imposed magnetic field strengths Λ. Also note that the subcritical branch always disappears for Λ greater than the critical Elsasser number at perfect resonance ($\delta = 0$).

The dependence of criticality on detuning is a well-known phenomenon for parametric instabilities that saturate through nonlinear phase-shifting. It was already

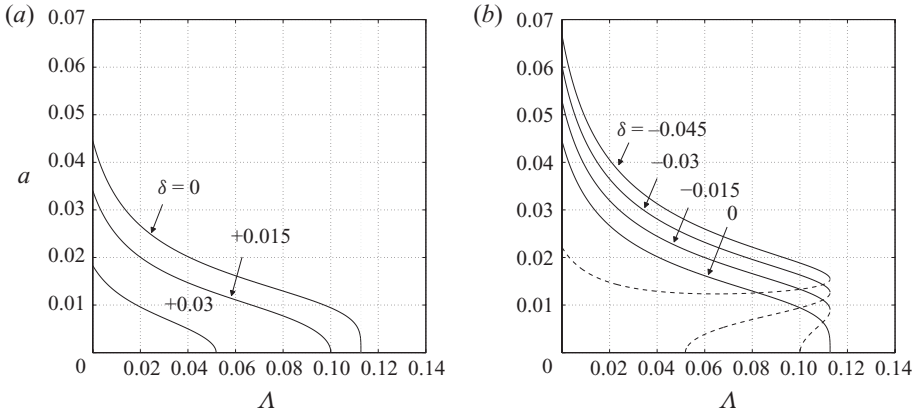

FIGURE 5. Theoretical bifurcation diagrams for the principal stationary mode amplitude a as a function of Elsasser number Λ for different values of the frequency detuning δ. Supercritical behaviour for positive detuning δ (a) and subcritical behaviour for negative δ (b). Stable (solid line) and unstable (dashed line) branches are indicated. Here, $E = 10^{-4}$, $\epsilon = 0.07$.

observed by Malkus (1989) in his original set-up, but it has been never mentioned again since then. Close to the linear instability threshold, small deviations Δh from the perfectly resonant aspect ratio h_* can lead to important changes in the amplitude of the excited flows.

In the experiments performed below, we use magnetic field damping in the same way as in figure 4. Having fixed ϵ, E and h, we perform successive experiments for varying magnetic field strength. Increasing the magnetic field strength, we approach the threshold, so that we can study the criticality of the bifurcation, and how this depends on small variations of the aspect ratio h. Note that experimental uncertainties such as misalignment errors will result in imperfect bifurcations. In supercritical cases $h > h_*$, we expect that the sharp threshold will be smoothed out by the noise. In subcritical cases $h < h_*$, finite-amplitude noise should be able to trigger the instability even when the system is linearly stable.

It is further interesting to see how the weakly nonlinear dynamics for the mode $(-1, 1, 1)$ would reflect in the recorded signals of the radial magnetic field components b_1 and b_2. The induced fields b_1 and b_2 are calculated with (3.19) at $(s, \phi, z) = (1, \pm\pi/4, 3)$. Both quantities are plotted together in the phase diagrams of figure 6, calculated with (3.36) and (3.37) and $\epsilon = 0.07$, $\Lambda = 0.02$, $E = 10^{-4}$ and for different values of δ. The trajectories leave the origin along a phase-angle $\arctan(b_2/b_1)$ that is mainly controlled by the frequency detuning δ, as described in (3.35). After this, they all spiral anticlockwise towards stable fixed points. The phase angle at saturation is independent of the detuning δ in the present weakly nonlinear model.

In the experiments of E03, saturated states are no longer observed beyond $E = 2.5 \times 10^{-4}$ for $\epsilon = 0.1$ and $h \simeq 8$. Saturated secondary instabilities, competing primary instability modes, but also growth-collapse-relaminarization cycles have been reported. However, quantitative measurements with Kalliroscope, are no longer simple to perform nor easy to interpret in these regimes. One of the objectives of this study is to use another diagnostic, e.g. the magnetic field induction, to monitor the dynamics of the flow and to analyse the transition from weakly nonlinear regimes to more complex states. This is the subject of § 4.

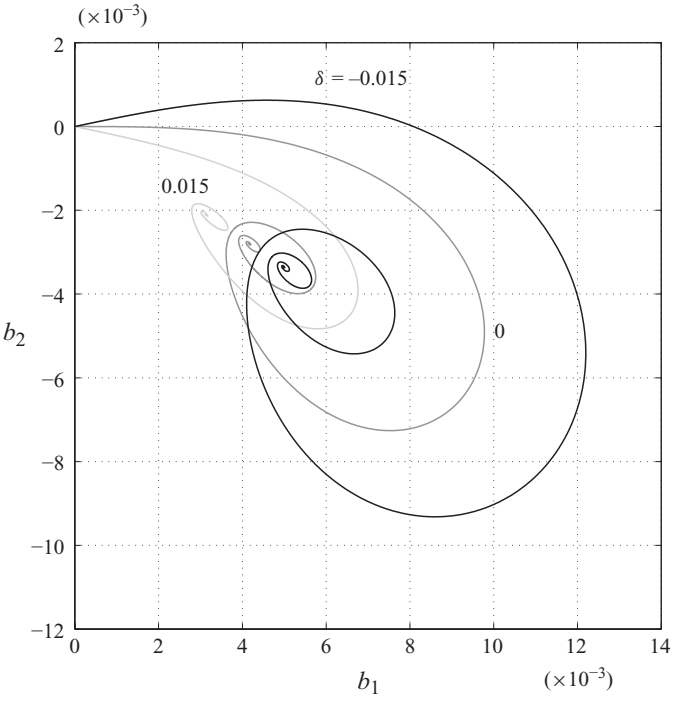

FIGURE 6. Phase diagrams obtained from the induced magnetic fields b_1 and b_2 for different values of the frequency detuning δ. Other parameters are fixed to $\epsilon = 0.07$, $E = 10^{-4}$, $\Lambda = 0.02$.

4. Experimental results

The experimental study mainly considers cylinders with an aspect ratio h close to 6. A typical experimental run in which only the imposed field is varied is presented in § 4.1. The analysis of the bifurcation is considered in § 4.2. Section 4.3 focuses on the effects of variable eccentricity and rotation rate on the dynamics of mean and fluctuating quantities when the system is far from threshold. Section 4.4 considers the evolution of another instability mode than the mode $(-1, 1, 1)$. In all the experiments, the magnetic field is rescaled with $[\boldsymbol{b}] = B_0\, Re_m$, so that the induced field reflects the amplitude of the perturbation flow.

4.1. *Example of a magnetically controlled transition*

Here, we fix the aspect ratio of the cylinder equal to $h = 148/25 = 5.92$. This case is close to the perfect non-viscous resonance condition for which $h_* = 5.97$. Rotation rate and eccentricity are also fixed such that $\epsilon = 0.15 \pm 0.01$, $Re_m = 0.0218$, $E = 1.58 \times 10^{-4}$. We calculate the frequency detuning as $\delta = -0.007$ and $\delta_{tot} = -0.002$ taking into account the viscous detuning. We expect to be close to perfect resonance conditions. The strength of the imposed magnetic field is changed such that Λ varies in the range $[0.20, 11.23] \times 10^{-2}$.

Figure 7 shows recorded time-series for strong to moderate imposed fields. As can be seen, for the strongest field ($\Lambda = 0.112$), the instability is suppressed. Below this value, the instability is present. The growth rate of the instability as well as the saturation level increase when the imposed field, that is Λ, decreases. When Λ becomes too small (here $\Lambda = 0.044$), the saturation no longer takes place and a regular limit cycle appears.

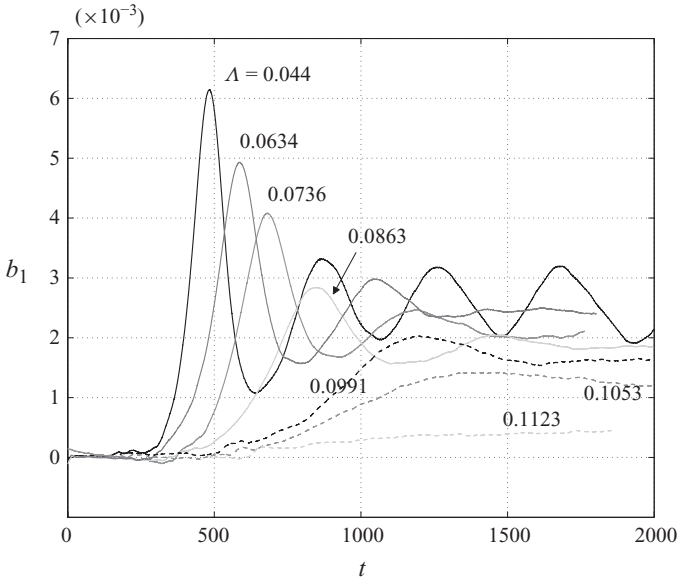

FIGURE 7. Experimental time series of b_1 for moderate-to-high Elsasser numbers Λ. Here, $h = 148/25$, $E = 1.58 \times 10^{-4}$, $\epsilon = 0.15$ and $\delta = -0.007$.

In figure 8, we show time series for both b_1 and b_2 together with their respective phase portraits for various Λ. For strong imposed fields ($\Lambda = 0.063$), we see how saturation takes place along a spiral in the (b_1, b_2) plane. Trajectories leave the origin downwards, as it would be the case for a supercritical bifurcation. At moderately imposed field ($\Lambda = 0.028$), the spiral structure in the (b_1, b_2) plane is still present, but the system does not saturate anymore and evolves to a slowly modulated limit cycle instead. A radical change is observed for weaker imposed fields ($\Lambda = 0.016$). After the initial growth along a 'fixed' direction in the phase plane, a sudden change of direction is observed leading to a change of sign of both magnetic components. This probably corresponds to a magnetic record of the collapse of the flow as it was seen by Eloy *et al.* (2003). After this reversal, the magnetic fields remain in a domain close to a fixed point and exhibits irregular oscillations. For very small imposed magnetic field ($\Lambda = 0.002$), the oscillations become sufficiently large to display several reversals/collapses. In the figure, we can see that when these reversals occur, the induced magnetic fields almost vanish, such that a linear growth phase can often be observed again.

Some quantitative results can also be obtained from the previous experimental signals. In figure 9(*a*), we show the growth rates measured for the initial growths observed in the different time series. Error bars are calculated from the deviations from each exponential fit. These deviations can become large, especially at low Λ. A linear fit of the different growth rates reveals a magnetic decay equal to -0.33Λ. Note that this value is higher than the theoretical value $-\Lambda/4$. The experimental growth rates are also typically smaller than the theoretical ones by a factor 2. This is not an effect of the magnetic field as it was also observed in a non-magnetic system by Eloy *et al.* (2003). We think that it could be associated with the non-homogeneity of the elliptic forcing which is applied only on two-thirds of the cylinder length(see Le Bars, Le Dizès & Le Gal 2007). No such discrepancy was observed in a spherical container (Herreman *et al.* 2009).

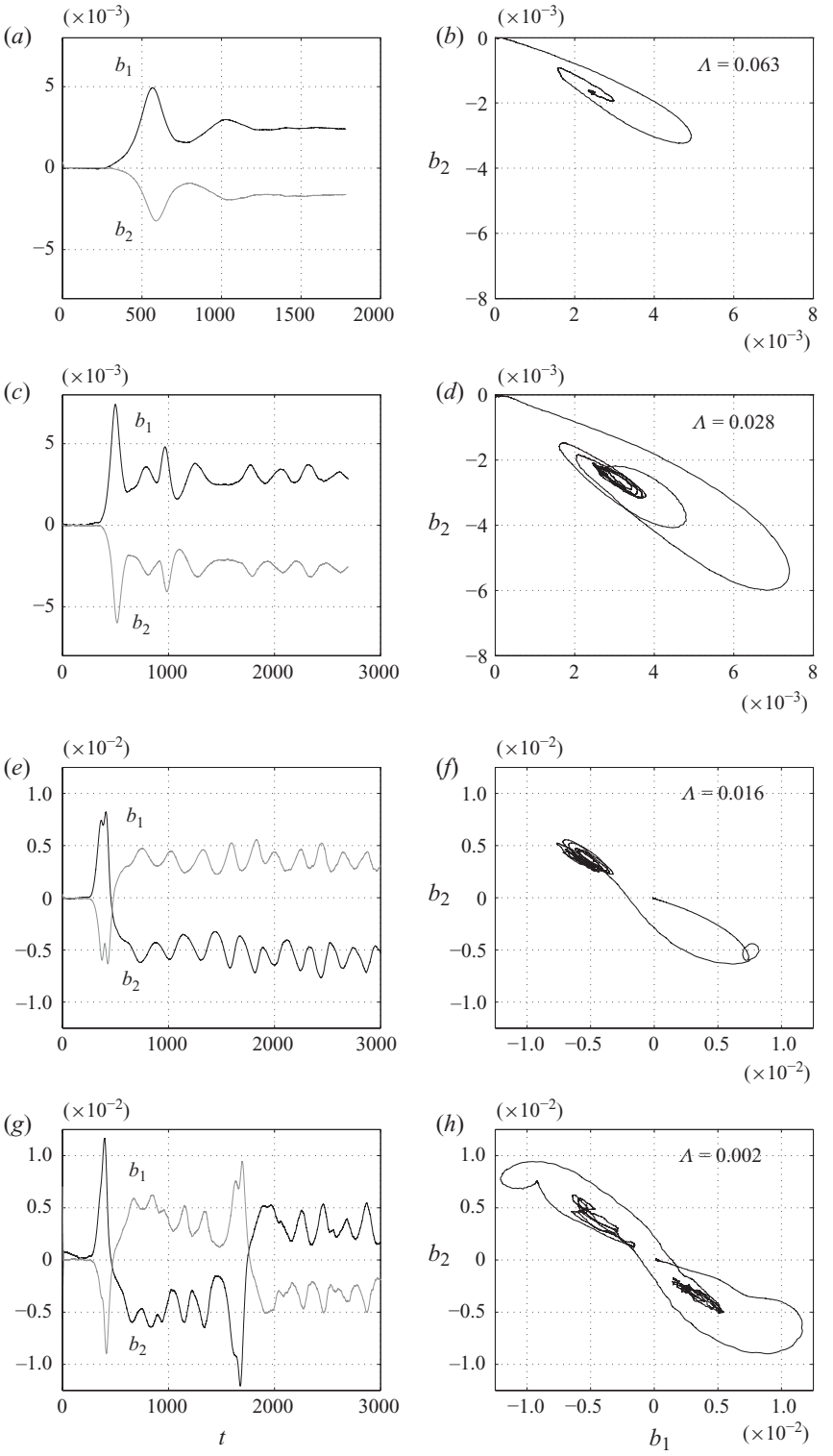

FIGURE 8. Experimental time series of the induced magnetic fields b_1 and b_2 together with the corresponding phase diagrams for different values of the Elsasser number Λ. Here, $h = 148/25$, $E = 1.58 \times 10^{-4}$ and $\epsilon = 0.15$.

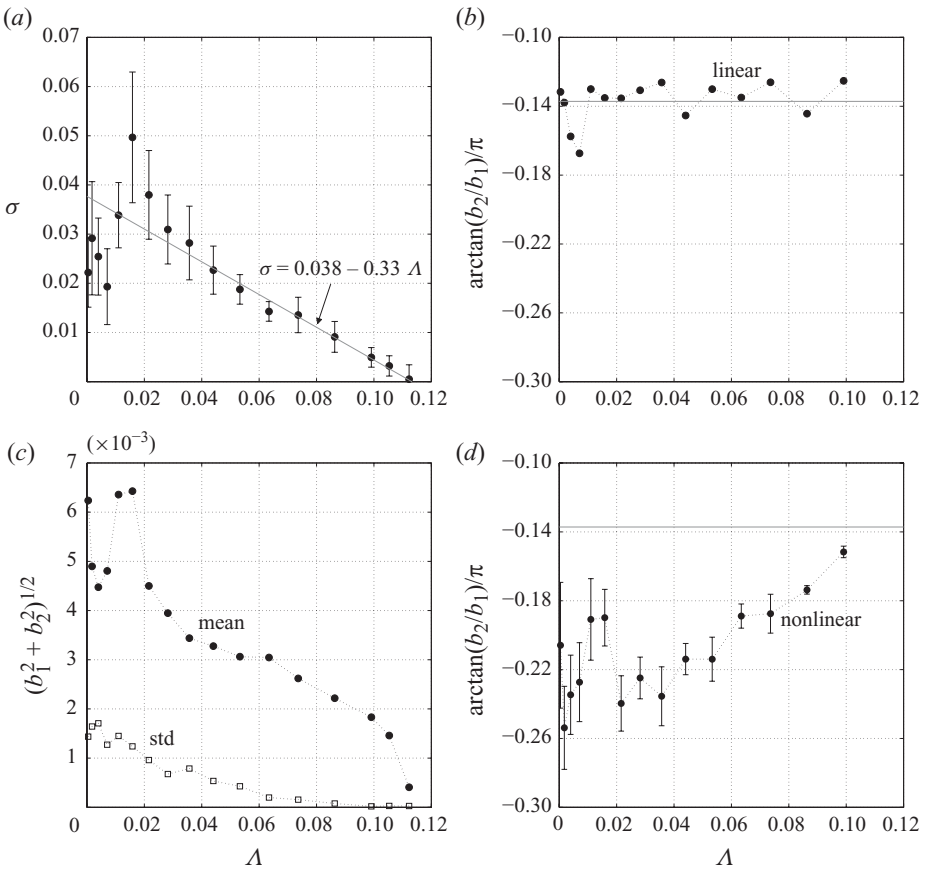

FIGURE 9. Characteristics of the principal stationary mode as a function of the Elsasser number. (*a*) Linear growth rate σ. A linear fit for $\Lambda > 0.02$ is also drawn with a grey line. (*b*) Linear phase angle $\arctan(b_2/b_1)/\pi$. (*c*) Mean value (●) and standard deviations (□) of $(b_1^2 + b_2^2)^{1/2}$. (*d*) Mean phase angle in the nonlinear regime.

In figure 9(*b*), the phase angle $\arctan(b_2/b_1)$ of the initial exponential phase of growth is plotted. We can see that the imposed magnetic field does not change the phase of the linearly unstable coupling in agreement with the theory. In figure 9(*c*), we show mean values (●) and standard deviations (□) of $(b_1^2 + b_2^2)^{1/2}$. This quantity can be seen as a measure of the mode magnitude a. Both mean and fluctuating parts of $(b_1^2 + b_2^2)^{1/2}$ gradually decrease as Λ increases. Close to the highest Λ, the mean amplitude falls down along a pitchfork. The figure is again close to what we would find for a supercritical bifurcation. Figure 9(*d*) shows the mean phase angle (●) and its standard deviations (bars) as a function of the Elsasser number Λ. As expected for a supercritical case, the observed phase angle at saturation, aligns better with the linearly predicted angle as the instability threshold is approached.

Other experiments have been performed and similar transitions in the time-series have generally been observed as Λ is varied. However, in some runs we have observed time series that exhibit intermittent growth–collapse cycles, which seem to be more organized than usual and perhaps controlled by a chaotic low-dimensional attractor. Figure 10 presents a typical example where such intermittent reversals can be observed.

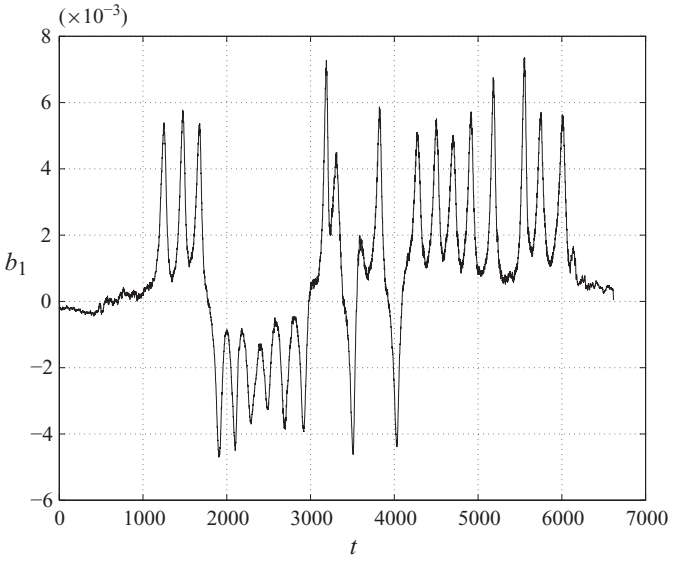

FIGURE 10. Observation of growth–decay cycles with chaotic reversals. Time series of b_1 in a cylinder of aspect ratio $h = 147/25$ for $\epsilon = 0.156$, $E = 1.18 \times 10^{-4}$ and $\Lambda = 4.9 \times 10^{-3}$.

4.2. *Criticality and frequency detuning*

In § 4.2, we focus further on the bifurcation and want to analyse the effect of the frequency detuning on the nature of the bifurcation. The experiments of § 4.1 suggested that elliptical instability in the cylinder $h = 148/25$ is supercritical. A further decrease of the aspect ratio should bring the system closer to a perfect resonance condition and to subcritical configurations.

We keep the same parameters $\epsilon = 0.15 \pm 0.01$, $E = 1.58 \times 10^{-4}$ as before and set the Elsasser number to $\Lambda = 0.0282$. Experiments are performed with two shorter cylinders: $h = 145/25$ where we find $\delta = -0.025$ and $\delta_{tot} = -0.020$ and $h = 142/25$, with $\delta = -0.044$ and $\delta_{tot} = -0.039$. The dynamics of the induced magnetic fields for the three different cylinders are compared in figure 11. We can see that the behaviour is similar for the three cases: it forms a spiral which converges towards a small amplitude limit cycle. However, the linear phase angle $\arctan(b_2/b_1)$ strongly varies from one case to the other. It is negative for the largest cylinder $h = 148/25$, as expected for a supercritical set-up, it is close to zero ($b_2 \simeq 0$) for $h = 145/25$, and becomes positive for $h = 142/25$. This last case corresponds to a subcritical bifurcation. This is confirmed experimentally as in fact we needed to add a finite-amplitude perturbation, a short pulse of eccentricity (+0.03), to initiate the growth of the linearly stable mode.

In figure 12, we display other measures that show subcritical behaviour. The cylinder has an aspect ratio $h = 145/25$ and $\epsilon = 0.15 \pm 0.1$, $E = 1.18 \times 10^{-4}$ and different Elsasser numbers Λ in the range $[0.0042, 0.1524]$ have been used. For these values, we have $\delta = -0.025$ and $\delta_{tot} = -0.021$.

In figure 12, only the signal from probe b_1 is plotted for seven values of Λ. The gradual decrease of the exponential growth with increasing Λ is again apparent, but we can also see that amplitudes at saturation make a sudden jump to a value close to zero in a short interval $[0.0951, 0.1054]$ of Λ. The time series for $\Lambda = 0.0951$, is clearly composed of two different phases showing that the instability growth is no longer purely exponential. For low Λ we found regular and irregular cycles as before,

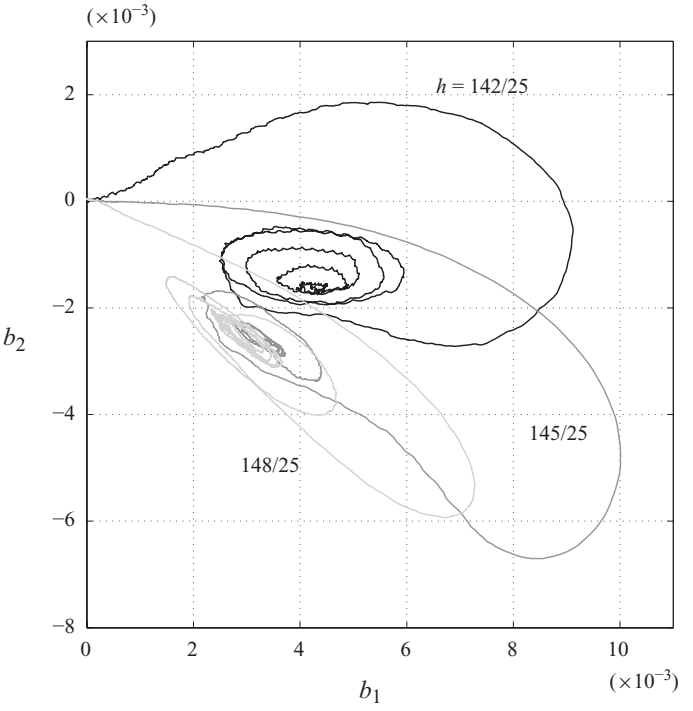

FIGURE 11. Phase portraits for the magnetic fields b_1 and b_2 for different aspect ratios $h = 148/25$, $145/25$, $142/25$, respectively, corresponding to frequency detunings $\delta = -0.007$, -0.025 and -0.044. All the other parameters are fixed: $\epsilon = 0.15$, $E = 1.58 \times 10^{-4}$ and $\Lambda = 0.0239$.

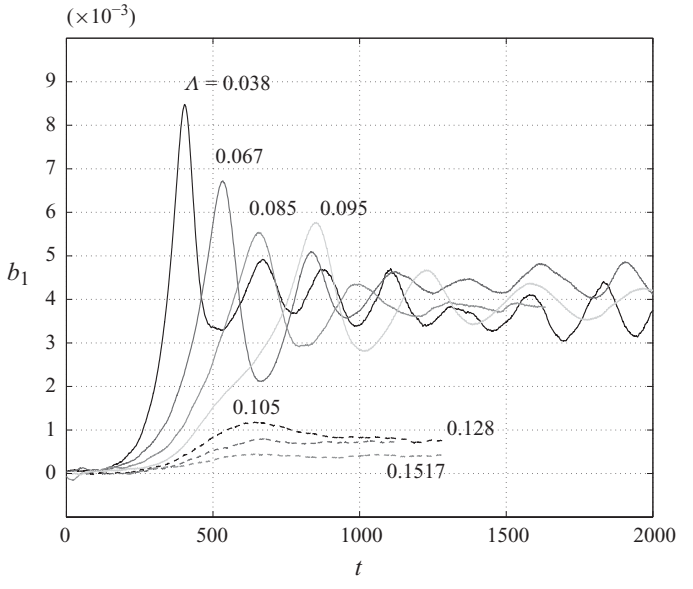

FIGURE 12. Experimental time series of b_1 for moderate-to-high Elsasser numbers Λ. Here, $h = 145/25$, $E = 1.18 \times 10^{-4}$, $\epsilon = 0.15$ and $\delta = -0.025$

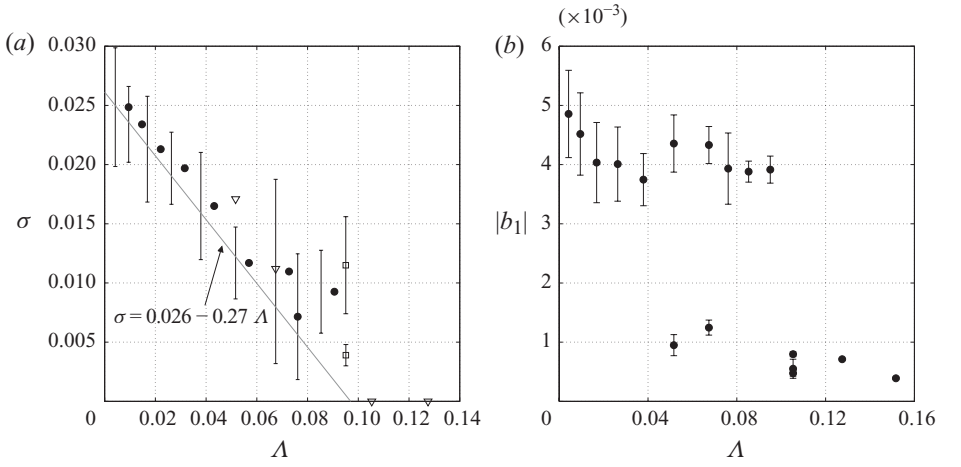

FIGURE 13. Variation of the growth rate (a) and saturation amplitude (b) of b_1 as a function of the Elsasser number Λ for $h = 145/25$, $E = 1.18 \times 10^{-4}$ and $\epsilon = 0.156$ as a function of Elsasser number Λ. In (b), both the mean saturation amplitudes (●) and typical oscillation amplitudes (bars) are indicated.

but no reversal. However, the polarity of the signal b_1 can be reversed between two different runs. The experiments have been repeated several times to test the robustness of the phenomena. Both low- and high-amplitude states have been found in the time series for $\Lambda = 0.0516$ and $\Lambda = 0.0674$. Such co-existing states are typical of imperfect subcritical bifurcations. For smaller values of Λ ($\Lambda < 0.0516$), we always observed high-amplitude solutions whereas the low-amplitude solutions were observed for larger values of Λ ($\Lambda > 0.0674$).

Quantitative information on the dynamics for the case considered in figure 12 can also be found in figure 13. Figure 13(a) shows linear growth rate measurements (●). Triangles (▽) are growth rates that were tentatively calculated for lower branch solutions. The two squares at $\Lambda = 0.0951$ correspond to the two distinct, but exponential parts of the growth. A linear fit that uses only the first six points reveals a magnetic damping coefficient equal to -0.27Λ, which is close to the theoretical value $-\Lambda/4$. However, growth rates do not go to zero in the same smooth way as in the previous supercritical case. For a subcritical case in the presence of noise, this is, however, not surprising. In figure 13(b), we show the mean (●) and the standard deviations (bars) of the signals from the probe b_1. Mean values do not vary much at low Elsasser number on both branches, but the sudden jump to the lower branch is clearly visible. Compared to the previous study for $h = 148/25$, we did not find a smooth decrease of the saturation amplitudes here. High saturation amplitudes are reached in the immediate vicinity of the linear instability threshold, as often expected in subcritical bifurcations.

4.3. *Effect of the eccentricity and of the Ekman number on the wave amplitude*

We have seen in § 4.2 that large amplitudes can be reached even close to threshold. In § 4.3, we want to analyse the dependence of this amplitude with respect to ϵ and E. In particular, we want to determine how saturation amplitudes scale on average with ϵ as we increase the distance from threshold. For this purpose, we have performed a series of experiments for different ϵ, in the same cylinder as before ($h = 145/25$), for $E = 1.58 \times 10^{-4}$ and small value of the Elsasser number ($\Lambda = 0.0057$). The time

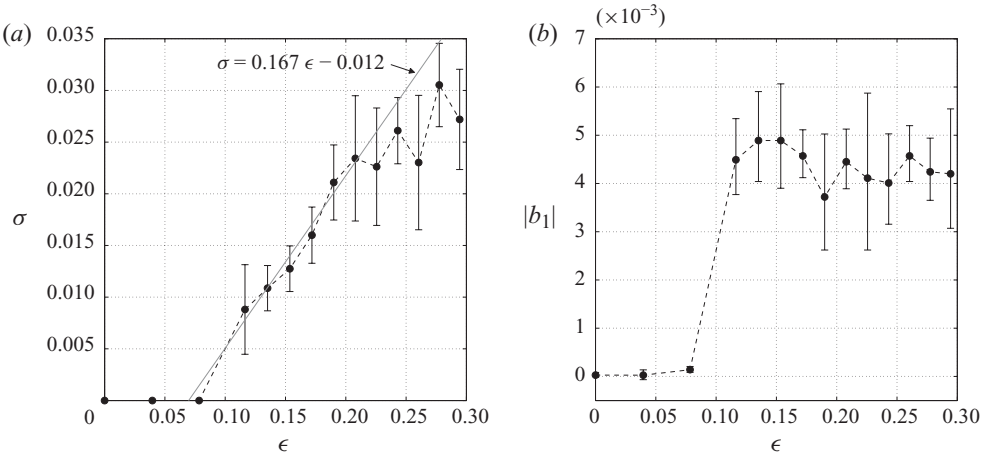

FIGURE 14. (*a*) Linear growth rate σ and (*b*) mean saturation amplitudes (●) and typical oscillation amplitudes (bars) as a function of the eccentricity ϵ. Here, $h = 145/25$, $E = 1.18 \times 10^{-4}$ and $\Lambda = 0.0057$. In (*a*), the dashed line represents a linear fit of the first six non-zero growth rates.

series obtained for this case (not shown here) are qualitatively similar to those shown above. In figure 14(*a*), the growth rate measured during the linear growth phase for different ϵ is plotted. We can see that the growth rate varies linearly with respect to ϵ as expected from the linear theory. However, a fit of the data gives a slope equal to 0.167 whereas the linear analysis predicts 0.531. This quantitative disagreement was already mentioned above and is probably due to an overestimation of the elliptic deformation in the experiment. In figure 14(*b*), the mean saturation amplitude of b_1 together with the standard deviation is plotted. As observed, there is a jump to a large value of the saturation amplitude as soon as the flow becomes unstable ($\epsilon \geqslant 0.1$). Moreover, this value does not seem to depend on ϵ. This suggests that the amplitude of the excited flow could be unrelated to ϵ. It is interesting to remark that similar behaviours were observed in the numerical simulations of Mason & Kerswell (2002) in the precessing plane fluid layer: kinetic energy of the weakly and strongly precessing branches is seemingly unrelated to the amplitude of the precessional perturbation in regimes far from the linear instability threshold.

If ϵ would not be the scaling parameter, we may wonder what controls the mean amplitudes of inertial waves far from threshold. To answer this question, we have performed another series of experiments with fixed imposed magnetic field $B = 110 \times 10^{-4}$ T, and fixed eccentricity $\epsilon = 0.15 \pm 0.1$ for varying rotation rates Ω in the range $[0.5, 2.5] \times 2\pi \,\mathrm{rad\,s^{-1}}$. For these rotation rates, the associated Ekman number E and magnetic Reynolds number Re_m vary in the intervals $[0.95, 4.73] \times 10^{-4}$ and $[0.007, 0.036]$, respectively. The Elsasser number Λ is small and lies in the interval $[0.0041, 0.0201]$. At low rotation rates, the time series are relatively smooth and close to the modulated limit cycles we have already described in figure 8(*b*). As the rotation rate increases, the signals become more irregular and start to display spikes and reversals as it was already observed in figure 8(*g*,*h*). Each experimental run was repeated several times. The imposed rotation direction was also reversed between different runs. This change of rotation exchanges the stretched and compressed axes, and therefore also the b_1 and b_2 signals. However, this exchange is not visible if we use $(b_1^2 + b_2^2)^{1/2}$ to describe the instability amplitude. In figure 15, we display the mean

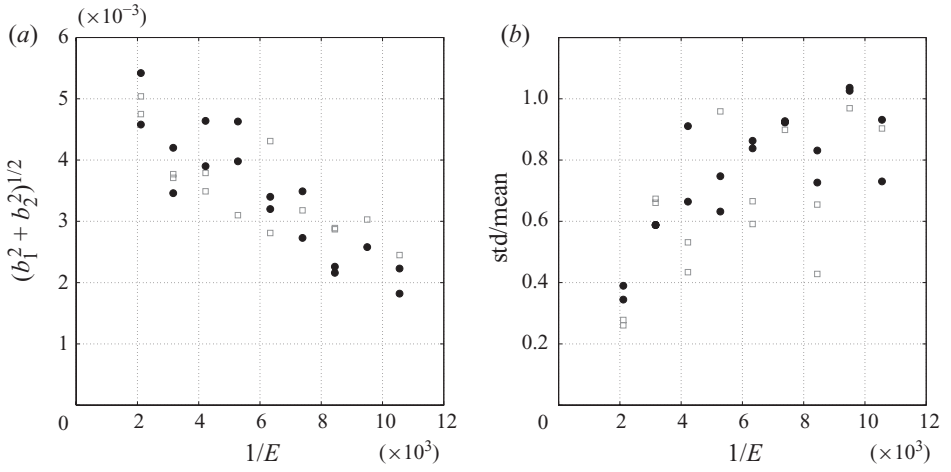

FIGURE 15. (*a*) Mean value and (*b*) fluctuation to mean ratio of $(b_1^2 + b_2^2)^{1/2}$ for increased rotation speed, measured by $1/E$. Here, $\epsilon = 0.15$ and $h = 145/25$. ●, positive rotation speed; □, negative rotation speed.

values of $(b_1^2 + b_2^2)^{1/2}$ (figure 15*a*) and the ratio of the standard deviation to the mean value (figure 15*b*) as a function of $1/E$. The direction of rotation of the set-up is also indicated for each measure. As observed in this figure, there is a large variance for the different experimental runs, but no clear difference between the two directions of rotation. We observe a global tendency for the mean amplitudes to decrease as the rotation speed increases. Standard deviations of the fluctuations increase gradually to reach values which are comparable to the mean amplitudes. This means that the growth collapse cycles reach larger and larger amplitudes. Therefore, even though the system is further from the linear instability threshold, the elliptically excited inertial wave cannot grow to the amplitude level that a weakly nonlinear theory would predict. We believe that secondary instabilities (Kerswell 1999; Eloy *et al.* 2003; Lagrange *et al.* 2008) come into play and diminish the amplitude of the stationary mode as E decreases. This regime could also be accompanied by an increased of the level of turbulence, but this was difficult to infer from our magnetic field measurements.

4.4. *Oscillatory modes*

In § 4.4, we consider the nonlinear dynamics of another mode than the mode $(-1, 1, 1)$. No data are currently reported in the literature for the nonlinear evolution of such modes. By tuning the aspect ratio to $h = 153/25$ or even to higher values, the mode $(-1, 1, 1)$ loses its predominance, and the resonant coupling $(1, 3, 1)$ sets in. This elliptical instability mode is composed of Kelvin waves of azimuthal wavenumbers $m = 1$ and $m = 3$, and has a frequency close to twice the angular velocity of the cylinder. In figures 16(*a*)–16(*c*), we show time series of b_1. Eccentricity was fixed to $\epsilon = 0.11$, and the rotation speed is doubled between each figure. Two signals are plotted in each figure corresponding to the instantaneous signal and its average value over 4 rotation periods. As can be seen, the instantaneous signal varies on a short time scale. The averaged signal reveals the long time-scale evolution. In figure 16(*a*) corresponding to the lowest rotation speed, we see rapid oscillations with an amplitude envelope that globally saturates. There is no clear evolution of the averaged signal. Doubling the rotation speed, we find the cycles which are presented in figure 16(*b*).

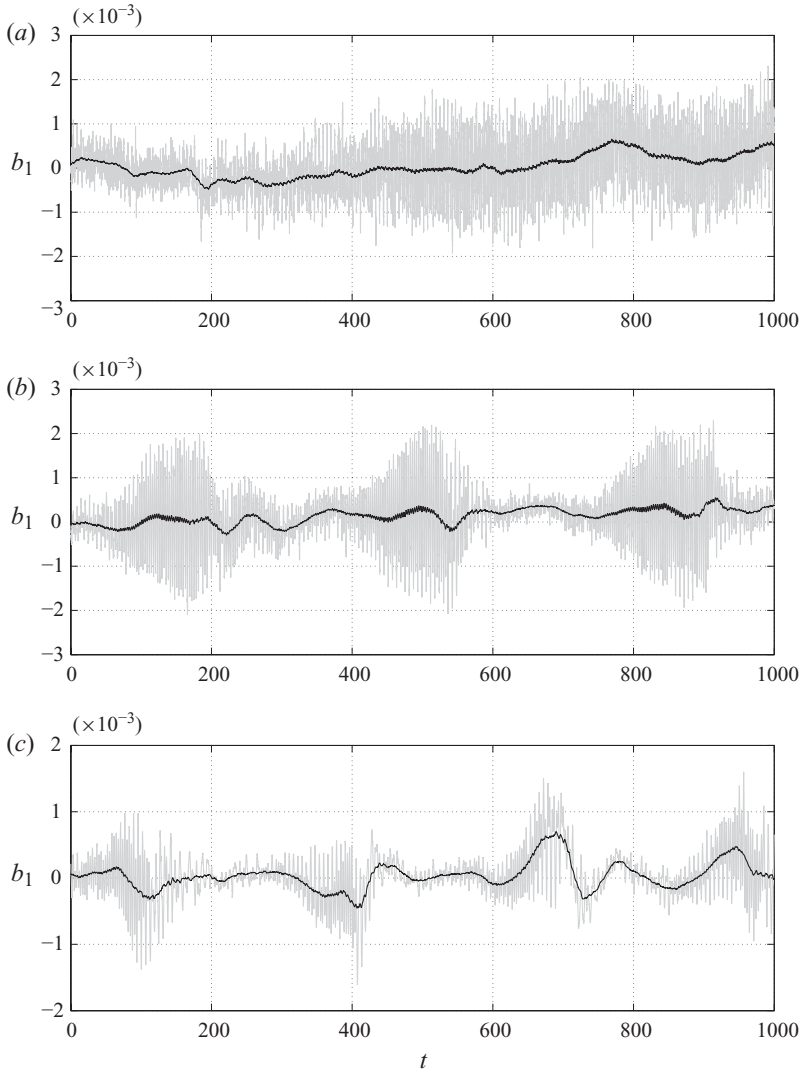

FIGURE 16. Time series (grey line) of b_1 and signal averaged over four rotation periods (black line) for $h = 153/25$ and $\epsilon = 0.156$. (*a*) $E = 4.73 \times 10^{-4}$ and $\Lambda = 4.03 \times 10^{-2}$ (*b*) $E = 2.36 \times 10^{-4}$ and $\Lambda = 2.38 \times 10^{-2}$, (*c*) $E = 1.18 \times 10^{-4}$ and $\Lambda = 1.01 \times 10^{-2}$.

The oscillation no longer saturates, but grows and abruptly disappears. The averaged signal still remains around zero. The frequency spectrum of this signal is plotted in figure 17, and exhibits a dominant peak at $\omega \simeq 2$ in agreement with what we expect for the resonance (1, 3, 1). Further doubling the rotation speed, we get figure 16(*c*). We still observe the rapid oscillating behaviour, but the signal has now a non-zero mean part that can acquire large amplitudes. Such slowly evolving signals are necessarily produced by flows that are stationary in the fixed frame, and besides the stationary modes $(-1, 1, i)$, there are not many other candidates of inertial waves that could be excited by elliptical instability. In fact, at $h = 153/25$, we are not far away from the resonant peak of the principal mode $(-1, 1, 1)$, and we think that this mode competes with the oscillatory signals of the (1, 3, 1) mode. Note that in between different cycles, the mean part of the signal can reverse in an intermittent way, just like in figure

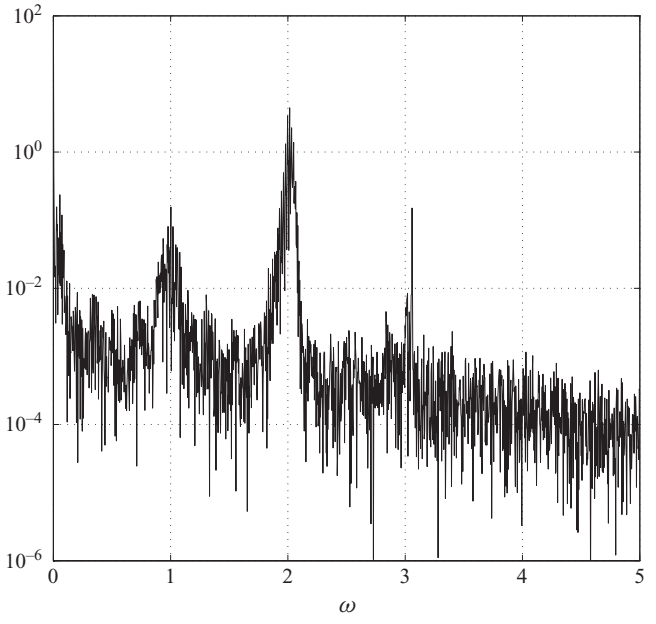

FIGURE 17. Frequency spectrum of the time series of figure 16(*b*). The frequency $\omega \simeq 2$ clearly corresponds to the dominant peak.

10. It is also interesting to see that the nonlinear evolution of the envelopes behaves qualitatively similarly to what we observed for the principal stationary mode (see figure 8).

5. Conclusion

This study demonstrates that a magnetic field can be used to measure and control a liquid metal flow. We have presented our experimental set-up, called IMAGINE, and we have developed theoretical arguments that allow the interpretation of magnetic field measurements as flow data. Both long and short time-scale evolutions are accessible, and high-quality data can be obtained.

Moreover, for the principal stationary mode $(-1, 1, 1)$ of the elliptical instability, we have shown that Joule damping can be used to control the transition to complex nonlinear dynamics which is described for the first time through experimental phase-portraits. In most of the experimental runs, the magnetically controlled transition scenario, starts with saturated states at high imposed field. Decreasing the field, limit cycles appear. These cycles are first regular and then irregular. Hydrodynamical reversals have been observed when the flow amplitude passes in the vicinity of the saddle point located at the origin.

We have also described the possibility of subcritical bifurcation for elliptical instability in finite fluid domains. This kind of subcritical behaviour is generic of parametric instabilities and is controlled by the sign of the frequency detuning. Close to the linear instability threshold, small detuning differences can result in very significant amplitude differences.

We have also observed that the eccentricity ϵ is not the appropriate quantity to estimate flow amplitudes far from threshold, at least not in the parameter regimes that were studied here. As a consequence, scaling arguments often used in geophysical

situations where the tidally generated flow is estimated either as $O(\epsilon)$ when instability is not considered or as $O(\epsilon^{1/2})$ in the presence of instability have to be applied with caution. We have seen that $O(1)$ flow can be generated by $O(\epsilon)$ elliptic deformation.

This work was funded by a PhD scholarship of the Ministère de la Recherche Française, and by the French National Agency for Research (ANR) under grant ANR-07BLAN-0182 (Project IMAGINE). The authors are grateful to H. Bouchiat who kindly provided the Helmholtz coils.

Appendix A. Matrix elements for the linear theory

The elliptic matrix elements E_{12} and E_{21} are identical to the non-viscous values found by Waleffe (1989), since inertial waves are unmodified. They can be written as $E_{12} = e_{12}/n_1$ and $E_{21} = e_{21}/n_2$, with

$$e_{12} = +\frac{\mathrm{i}}{2}(2-\lambda_1)\left(4-\lambda_2^2\right)I, \tag{A 1}$$

$$e_{21} = -\frac{\mathrm{i}}{2}(2+\lambda_2)\left(4-\lambda_1^2\right)I, \tag{A 2}$$

$$n_1 = \frac{2}{k_1}(2+\lambda_1)J_m(k_1)J_{m-1}(k_1) + 4\left(J_m^2(k_1) - J_{m+1}(k_1)J_{m-1}(k_1)\right), \tag{A 3}$$

$$n_2 = \frac{2}{k_2}(2+\lambda_2)J_{m+2}(k_2)J_{m+1}(k_2) + 4\left(J_{m+2}^2(k_2) - J_{m+3}(k_2)J_{m+1}(k_2)\right), \tag{A 4}$$

and

$$\left.\begin{aligned} I &= \frac{1}{k_2^2-k_1^2}\left(k_1 J_m(k_1)J_{m+1}(k_2) - k_2 J_{m+1}(k_1)J_m(k_2)\right), && k_1 \neq k_2, \\ &= \tfrac{1}{2}\left(J_m(k_1)^2 - J_{m+1}(k_1)J_{m-1}(k_1)\right), && k_1 = k_2. \end{aligned}\right\} \tag{A 5}$$

The viscous corrections d_j^V in (3.29) contain a surface contribution and the volume damping due to the diffusive operator $\mathscr{V}$. Again, these terms are not different from previously derived expressions. Using Kudlick's estimate for the surface damping (Kudlick 1964), the viscous term is written down explicitly as

$$\begin{aligned} d^V = E^{1/2}\frac{4-\lambda^2}{4\sqrt{2}\,\left(m^2+l^2-m\lambda/2\right)}\Bigg[&(1+\mathrm{i})\lambda^{1/2}(m^2+l^2) \\ &+ \frac{(1+\mathrm{i})}{h}\frac{(2-\lambda)}{\sqrt{2+\lambda}}\left(m^2+l^2-\frac{2m\lambda}{2-\lambda}\right) + \frac{(1-\mathrm{i})}{h}\frac{(2+\lambda)}{\sqrt{2-\lambda}}\left(m^2+l^2-\frac{2m\lambda}{2+\lambda}\right)\Bigg] \\ &+ E(k^2+l^2). \end{aligned} \tag{A 6}$$

The principal stationary mode $(-1, 1, 1)$ is perfectly resonant in a cylinder with aspect ratio $h_* = 5.9694$ with $n = 3$ vertical wavelengths in its vertical structure. It is composed of a mode with wavenumbers $(k, m, l, \omega) = (2.7346, 1, 1.5788, 0)$ and its complex conjugate. The elliptical matrix element is $E_{1,-1} = -0.5312\mathrm{i}$. The viscous damping $d^V = (0.8962 + 0.3928\mathrm{i})\,E^{1/2} + 9.9709\,E$.

Appendix B. Matrix elements for the weakly nonlinear model

The parameters of the nonlinear model (Eloy *et al.* 2003), used in (3.36) and (3.37) are repeated here for practical reasons. The inviscid growth rate is $\sigma_i = 0.5312$. The

j	$K^{(j)}$	$\xi^{(j)}$	$\lambda_1^{(j)}$	$\lambda_1^{(j)}$
1	3.83	−0.223	−18.47	43.5
2	7.01	−0.153	−3.33	9.36
3	10.2	0.056	0.76	−2.64
4	13.3	−0.033	−0.33	1.45

TABLE 1. Coefficients of the weakly nonlinear model of Eloy *et al.* (2003), for the weakly nonlinear evolution of the principal stationary mode (−1, 1, 1) in a cylinder with aspect ratio $h = 8$. See also (3.36) and (3.37).

nonlinear coefficient is $D = 2.015$. The damping coefficients are $\mu_0 = 0.801 + 9.97E^{1/2}$, $\mu_1^{(j)} = 0.125 + K^{(j)}\,E^{1/2}$. The parameters $K^{(j)}$, $\xi^{(j)}$, $\lambda_1^{(j)}$, $\lambda_1^{(j)}$ are given in table 1, for the first four geostrophic modes $j = 1, \ldots, 4$. The fast decreasing behaviour of λ_1^j, λ_2^j and ξ^j justifies the use of no more than four geostrophic modes.

REFERENCES

BAYLY, B. J. 1986 Three-dimensional instability of elliptical flow. *Phys. Rev. Lett.* **57**, 2160–2163.

ELOY, C., LE GAL, P. & LE DIZÈS, S. 2003 Elliptic and triangular instabilities in rotating cylinders. *J. Fluid Mech.* **476**, 357–388.

HERREMAN, W., LE BARS, M. & LE GAL, P. 2009 On the effects of an imposed magnetic field on the elliptical instability in spheroids. *Phys. Fluids* **21**, 46602.

KELLEY, D. H., TRIANA, S. A., ZIMMERMAN, D. S., TILGNER, A. & LATHROP, D. P. 2007 Inertial waves driven by differential rotation in a planetary geometry. *Geophys. Astrophys. Fluid Dyn.* **101**, 469–487.

KELVIN, LORD 1880 Vibrations of a columnar vortex. *Phil. Mag.* **10**, 155–168.

KERSWELL, R. R. 1993 Elliptical instabilities of stratified, hydromagnetic waves. *Geophys. Astrophys. Fluid Dyn.* **71**, 105–143.

KERSWELL, R. R. 1994 Tidal excitation of hydromagnetic waves and their damping in the Earth. *J. Fluid Mech.* **274**, 219–241.

KERSWELL, R. R. 1999 Secondary instabilities in rapidly rotating fluids: inertial wave breakdown. *J. Fluid Mech.* **382**, 283–306.

KERSWELL, R. R. 2002 Elliptical instability. *Annu. Rev. Fluid Mech.* **34**, 83–113.

KERSWELL, R. R. & MALKUS, W. V. R. 1998 Tidal instability as the source for Io's magnetic signature. *Geophys. Res. Lett.* **25**, 603–606.

KUDLICK, D. 1964 On the transient motion. *J. Math. Phys.* **5**, 963–982.

LACAZE, L., HERREMAN, W., LE BARS, M., LE DIZÈS, S. & LE GAL, P. 2006 Magnetic field induced by elliptical instability in a rotating spheroid. *Geophys. Astrophys. Fluid Dyn.* **100**, 299–317.

LAGRANGE, R., ELOY, C., NADAL, F. & MEUNIER, P. 2008 Instability of a fluid inside a precessing cylinder. *Phys. Fluids* **20** (8), 081701.

LE BARS, M. & LE DIZÈS, S. 2006 Thermo-elliptical instability in a rotating cylindrical shell. *J. Fluid Mech.* **563**, 189–198.

LE BARS, M., LE DIZÈS, S. & LE GAL, P. 2007 Coriolis effects on the elliptical instability in cylindrical and spherical rotating containers. *J. Fluid Mech.* **585**, 323–342.

LEBOVITZ, N. R. & ZWEIBEL, E. 2004 Magnetoelliptic instabilities. *Astrophys. J.* **609** (1), 301–312.

LEWEKE, T. & WILLIAMSON, C. H. K. 1998 Cooperative elliptic instability of a vortex pair. *J. Fluid Mech.* **360**, 85–119.

MALKUS, W. V. R. 1989 An experimental study of global instabilities due to tidal (elliptical) distortion of a rotating elastic cylinder. *Geophys. Astrophys. Fluid Dyn.* **48**, 123–134.

MANASSEH, R. 1992 Breakdown regimes of inertia waves in a precessing cylinder. *J. Fluid Mech.* **243**, 261–296.

MASON, D. M. & KERSWELL, R. R. 1999 Nonlinear evolution of the elliptical instability: an example of inertial wave breakdown. *J. Fluid Mech.* **396**, 73–108.

Mason, D. M. & Kerswell, R. R. 2002 Chaotic dynamics in a strained rotating flow: a precessing plane fluid layer. *J. Fluid Mech.* **471**, 71–106.

McEwan, A. D. 1970 Inertial oscillations in a rotating fluid cylinder. *J. Fluid Mech.* **40** (3), 603–640.

Miyazaki, T. 1993 Elliptical instability in a stably stratified rotating fluid. *Phys. Fluids* A **5** (11), 2702–2709.

Mizerski, K. A. & Bayer, K. 2009 The magnetoelliptic instability of rotating systems. *J. Fluid Mech.* **632**, 401–430.

Racz, J.-P. & Scott, J. F. 2008 Parametric instability in a rotating cylinder of gas subject to sinusoidal axial compression. Part 2. Weakly nonlinear theory. *J. Fluid Mech.* **595**, 291–321.

Schaeffer, N. & Le Dizès, S. 2010 Nonlinear dynamics of the elliptic instability. *J. Fluid Mech.* **646**, 471–480.

Schmitt, D., Alboussière, T., Brito, D., Cardin, P., Gagnière, N., Jault, D. & Nataf, H.-C. 2008 Rotating spherical Couette flow in a dipolar magnetic field: experimental study of magneto-inertial waves. *J. Fluid Mech.* **604**, 175–197.

Sipp, D. 2000 Weakly nonlinear saturation of short-wave instabilities in a strained Lamb–Oseen vortex. *Phys. Fluids* **12** (7), 1715–1729.

Stefani, F., Gundrum, T., Gerbeth, G., Rüdiger, G., Schultz, M., Szklarski, J. & Hollerbach, R. 2006 Experimental evidence for magnetorotational instability in a Taylor–Couette flow under the influence of a helical magnetic field. *Phys. Rev. Lett.* **97** (18), 184502.

Thess, A. & Zikanov, O. 2007 Transition from two-dimensional to three-dimensional magnetohydrodynamic turbulence. *J. Fluid Mech.* **579**, 383–412.

Vladimirov, V. A & Vostretsov, D. G. 1986 Instability of steady flows with constant vorticity in vessels of elliptic cross-section. *Prikl. Mat. Mekh. U.S.S.R.* **50** (3), 279–285.

Waleffe, F. 1989 The 3D instability of a strained vortex and its relation to turbulence. PhD thesis, Massachusetts Institute of Technology, Cambridge, MA.